ANNALS OF GEOPHYSICS, 68, 3, NS337, 2025; doi:10.4401/ag-9251
OPEN ACCESS

Characterizing Seismic Response from Ground Motion Records: A Local-Scale Study for Geotechnical Applications

Gustavo Posada[*,1], Fernando Díaz-Parra[1], Julián Montejo[1]

(1) Servicio Geológico Colombiano, Bogotá, Colombia

Article history: received January 16, 2025; accepted June 20, 2025

Abstract

This study focuses on enhancing our understanding of sites dominated by both soil properties and complex topographic conditions by analyzing ground motion records collected by the Pereira Ground motion network. We implemented various techniques to investigate the site effects, including empirical site classes and their relative amplification. Additionally, the fragility index (Kg) was estimated using earthquake and microtremor data, enabling a comparison between the two approaches. Furthermore, we identified how the topographic conditions of the terrain modified the seismic response at station sites. This research aims to comprehensively understand site effects during seismic events by combining site classification, fragility assessment, and topographic analysis. The findings from this study have the potential to contribute to the development of effective strategies for seismic response zonation and assessment, building design, and seismic risk assessment from a site characterization perspective.

Keywords: Ground motion; Site effects; Response spectrum; Fourier spectrum; Relative amplification; Topographic effects; Site characterization

1. Introduction

Rupture parameters, path configuration, and local soil conditions primarily influence seismic intensities and ground motions observed during an earthquake at a specific location. The significance of site conditions in seismic studies has been extensively explored in the literature. The Mw 8.0 megathrust earthquake in México serves as a classic example of the profound influence of soil deposits on the behavior of seismic waves, including ground accelerations and velocities, particularly when compared to the effects observed in hard-rock regions. Researchers have reported significant amplification in Mexico City resulting from both distant and nearby seismic events (Reinoso and Ordaz, 1999). Knowledge of site effects, obtained through methods such as numerical modeling and analysis of historical events, is essential for seismic response zonation and comprehensive site characterization.

In Colombia, local soil conditions have similarly influenced the impact of destructive earthquakes, such as the Mw 5.6 Popayán earthquake in 1983 (Page, 1984) and the Mw 6.1 event in the Coffee Region in 1999 (Chávez-García et al., 2018). In response to such events, Colombia has mandated microzonation studies since the 1990s. These studies are required in capital cities and in cities with populations over 100,000 located in moderate to high seismic hazard regions. The goal of microzonation is to perform a comprehensive characterization of seismic

site conditions using empirical and numerical data to estimate expected seismic amplification and its implications for seismic design demands.

One example is the city of Pereira, located in the Coffee Region of Colombia. As the capital of Risaralda Department and situated in a high seismic hazard zone according to the current seismic building code (NSR-10), Pereira is on the Armenia fan, a geomorphological unit composed of Quaternary fluvio-volcanic sediments (Nelson, 1957). Below these surficial deposits, Caballero and Zapata (1984), report lithological variations, identifying Cretaceous rocks such as the Diabase Group (basalts, diabase, and pyroclastics), the Quebradagrande Formation (greywacke, chert, slate limestone, and conglomerate), and the Gabbroic stock of Pereira. Additionally, Paleozoic green and graphitic schists are also present. Furthermore, human activities have modified the local geology, with the implementation of landfills to reclaim land and facilitate neighborhood development. These conditions made Pereira a suitable candidate for microzonation studies, first conducted in 1999 and updated in 2019. Given that microzonation involves costly geotechnical and geophysical surveys and complex numerical modeling, this study explores simplified methodologies for site characterization using strong motion data. The goal is to evaluate whether a framework based on single-station strong motion records can be used to: categorize sites, assess site amplification, estimate seismic fragility, and investigate wave directivity. It is important to note that while this research provides valuable local-scale insights into seismic response and contributes to validating existing zonation, the localized distribution of the seismic stations means it serves as a complementary study and does not substitute for a detailed, comprehensive seismic microzonation of the entire urban area.

Recognizing the significant influence of local soil conditions, considerable effort has gone into identifying soil categories with homogeneous seismic responses. The initial approach involved a binary classification of soil versus rock sites. A more refined and quantitative parameter, the shear-wave velocity to a depth of 30 meters (Vs_{30}), has since emerged. Vs_{30}, correlated with geotechnical properties, is a reliable proxy for seismic amplification and has become a standard parameter in seismic design codes globally, especially since its inclusion in American code provisions (Building Seismic Safety Council (US), 1988; International Council of Building Officials (ICBO), 1997) More recently, empirical site classification through the Horizontal-to-Vertical Response Spectral Ratio (HVRSR) has gained popularity. Specifically, the classifications proposed by Zhao et al. (2006), Fukushima et al. (2007), Di Alessandro et al. (2012), and Idini et al. (2017) have demonstrated the effectiveness of HVSR-based site categories. Although these were developed for regional contexts, their application in Colombia has shown promising results on both local (Posada et al., 2022) and regional scales (Arteta et al., 2021, 2023; Mercado et al., 2023).

Beyond site classification, various methods exist to evaluate site response and site characteristics using ground motion recordings. One such method is the ground fragility index (K_g), which helps to evaluate the risk of soil liquefaction (Nakamura, 2019). This method typically uses microtremor data to compute the Horizontal-to-Vertical Fourier Spectral Ratio (HVFSR), relating amplitude to resonance frequency. Although originally designed for ambient noise, we applied this method to earthquake data and compared the results. Another approach is the direct calculation of seismic amplification by comparing ground surface recordings with those from rock layers obtained from borehole sensors (Kokusho and Sato, 2008). However, such borehole data are scarce in Colombia.

Site conditions are closely linked to the configuration of subsurface soil layers, typically simplified as a one-dimensional problem. However, two- and three-dimensional effects can significantly influence seismic response. These effects arise from the interaction of vertically propagating (e.g., their conversion to surface waves) and from complex subsurface geometries (Pilz and Cotton, 2019). Topographic effects fall into this category, as natural features such as hills can alter seismic response. For instance, the top of a slope can exhibit greater amplification, and spectral amplitudes can vary with azimuth, leading to directional resonance along the steepest slope (Massa et al., 2014). Researchers have used ground motion and ambient noise data to study these effects, applying rotated Fourier spectra to detect azimuth-dependent amplification (Massa et al., 2014; Panzera et al., 2013; Pischiutta et al., 2012). In the time domain, polarization analysis of the covariance matrix (Jurkevics, 1988) provides a visual trend of horizontal motion direction, allowing identification of directional resonance angles.

This study presents a comprehensive analysis of various techniques applied to ground motion records to enhance our understanding of soil seismic response. Our methodology consists of three main steps to perform a practical geophysical site characterization using accelerograph data. First, we determined empirical site classes for the Pereira stations and calculated their relative amplification to assess local site effects. Second, we estimated the fragility index (K_g) using both earthquake and microtremor data, highlighting similarities and differences. Finally,

we evaluated how topographic features, such as slope and elevation, affect seismic response. By integrating these approaches, we aim to develop a cost-effective framework that contributes to a more holistic understanding of soil behavior during earthquakes and supports future research and decision-making.

2. Applied Methods

This study employs strong motion records from accelerograph stations in Pereira. All recorded data underwent standard preprocessing to ensure data quality. Specifically, detrending was performed using the 'simple' method implemented in the "obspy.core.trace.Trace.detrend" function from the ObsPy library (Beyreuther et al., 2010). Subsequently, a 5% Hamming taper was applied, and the data were filtered using an 8^{th}-order zero-phase band-pass Butterworth filter between 0.08 and 20 Hz. For earthquake-specific analyses, signals were further examined to delineate pre-event noise, P-wave and S-wave arrivals, and the coda wave. This paper then presents four different methodologies for evaluating the seismic response behavior of soils: i) empirical site classification, ii) empirical transfer functions, iii) K_g vulnerability index, and iv) horizontal terrain directional analysis.

2.1 Empirical site classification

We used 5% damping response spectra to generate the horizontal-to-vertical response spectral ratios (HVRSR). For calculating the spectral ratio, we used the geometric mean of the response spectra of both horizontal components as a proxy for the horizontal movement. We then calculated the quotient between this horizontal component and the vertical spectrum. The geometric mean was chosen to represent horizontal intensity because it is an intensity measure commonly used to represent ground shaking (Bradley and Baker, 2015). Additionally, this metric reduces the aleatory uncertainty for ground motion prediction (Beyer, 2006), making it one of the most widely adopted metrics for ground motion practices globally. We applied the Newmark-Beta method for the response spectrum calculation using the Python package GMPE-smkt (Weatherill et al., 2014). The response spectra were calculated between 0.08 and 3 seconds, and then we averaged the resulting HVRSR curves to obtain a single representative curve for each station.

The characteristics of the HVRSR curve, particularly its peak, provide the fundamental period of the site. Several authors have applied the HVRSR method to establish empirical site classifications (Di Alessandro et al., 2012; Fukushima et al., 2007; Idini et al., 2017; Zhao et al., 2006). Table 1 summarizes classes defined by each author. While these classifications often exhibit similar period ranges for some categories, Idini's (2017) classes notably group periods between 0.4 and 0.8 s and introduce the P* parameter to differentiate amplitude values.

Table 1. Empirical site classifications implemented in different countries using HVRSR curves. T is the site's natural period inferred from HVRSR. P* indicate the amplitude of the HVRSR.

Site Categories							
Zhao et al. (2006)		Fukushima et al. (2007)		Di Alessandro et al. (2012)		Idini et al. (2016)	
Site class	Description	Site class	Description	Site class	Description	Site class	Description
SC-I	$T < 0.2$ s	SC-1	$T < 0.2$ s	CL-I	$T < 0.2$ s	S_I	Not identifiable: HVRSR < 2
SC-II	$0.2 \text{ s} \leq T < 0.4$ s	SC-2	$0.2 \text{ s} \leq T < 0.4$ s	CL-II	$0.2 \text{ s} \leq T < 0.4$ s	S_{II}	$T^* \leq 0.2$ s
SC-III	$0.4 \text{ s} \leq T < 0.6$ s	SC-3	$T > 0.4$	CL-III	$0.4 \text{ s} \leq T < 0.6$ s	S_{III}	$0.2 \text{ s} < T^* \leq 0.4$ s

Site Categories							
Zhao et al. (2006)		Fukushima et al. (2007)		Di Alessandro et al. (2012)		Idini et al. (2016)	
Site class	Description	Site class	Description	Site class	Description	Site class	Description
SC-IV	T > 0.6	SC-4	Not identifiable (rock site)	CL-IV	T > 0.6	S_{IV}	0.4 s < T* ≤ 0.8 s
—		SC-5	Not identifiable (soil site)	CL-V	Not identifiable (flat HVRSR and amplitude <2)	S_V	T* > 0.8
—		—	—	CL-VI	Multiple peaks at T < 0.2 s	S_{VI}	Not identifiable: BB amplification or 2+ peaks
—		—	—	CL-VII	T not identifiable (Multiple peaks over entire period range)	**Classes for P***	**P***
						A	2 ≤ P* < 3
						B	3 ≤ P* < 4
						C	P* ≥ 4

2.2 Empirical transfer function

We calculated the empirical transfer function (ETF) for periods between 0.08 and 3 seconds to estimate the relative spectral amplification to a reference site. To estimate these amplification functions, we calculated the quotient between the horizontal response spectra as follows:

$$ETF = S_{hs}/S_{hr} \quad (1)$$

where, S_{hs} and S_{hr} correspond to the site's horizontal spectra (through the geometric mean of both horizontal components) and the reference on the same component (Borcherdt, 1970, 1994). In this case, the *CL-V* class defines the reference site due to the closest to the hard-rock conditions.

These estimations are helpful for the calibration and validation process in 1D and 2D numerical models. Since the 1D and 2D models performed in software such as Deepsoil (Hashash et al., 2020) or Quad4M (Hudson and Idriss, 1994) consist of simplified layered models with Vs, densities, damping, and soil degradation curves, where the propagation of seismic waves from the bedrock to the surface level is modeled. The comparison with empirical amplification functions lets the numerical model be appropriately validated to represent the real site effects (Farrugia et al., 2018; Kaklamanos et al., 2015).

2.3 Vulnerability index (K_g)

The K_g index is implemented by directly calculating the HVFSR spectra to assess the stiffness of subsoil and the potential damage during an earthquake (Nakamura, 2019). Nakamura and Takizawa (1990b) (Nakamura, 2019) defined this parameter as the quotient between natural frequency (F) and its peak amplitude (A) from the HVFSR of ambient noise:

$$K_g = A^2/F \quad (2)$$

To Calculate this index, we generated H/V curves like HVFSRs, where we merged the horizontal components of Fourier spectra through geometric mean and later the quotient between combined and vertical spectra. Then, we generated the averaged curves with their respective standard deviations. K_g is a vulnerability index and has been successfully correlated with high-damage regions during historical seismic events, including those that occurred in 1957, 1979, and the 1985 earthquakes over Mexico City, as well as the effects of the 1995 Hyogo-Ken-Nanbu earthquake over Kobe (Nakamura, 2002). Furthermore, K_g has shown consistency with the parameters commonly used for site effects evaluation, and this is the case of Vs_{30}, which is inversely proportional to the Kg index (Akkaya, 2020; Kang et al., 2022; Pamuk et al., 2018) and the natural frequency included directly on Kg estimation.

Despite its good performance in estimating the seismic site conditions, the principal use of the K_g index since its formulation probably has been the soil liquefaction assessment. Several examples in the literature of this method are from traditional geotechnical information, such as SPT tests and the cyclic resistance ratio (CRR) (Abdelrahman et al., 2022; Jalil et al., 2021; Rezaei and Choobbasti, 2014). The K_g value is primarily correlated with soil liquefaction and damage to small buildings, as previously remarked by Nakamura (2019). Additionally, low K_g values typically correspond to hard soils or soft rocks whose seismic response is at low periods and amplifications, while high values of Kg are related to soft soils and deeper with the seismic response at high periods (Güven, 2022; Meneisy et al., 2020).

2.4 Horizontal terrain directional analysis

We implemented methodologies in the time and frequency domains to evaluate topographic effects. The frequency domain method involves the horizontal-to-vertical ratio from the Fourier spectrum (HVFSR) as a function of both frequency and direction of movement (Pischiutta et al., 2022). Previous studies (Di Giulio et al., 2009; Massa et al., 2014; Panzera et al., 2013; Pischiutta et al., 2012) have implemented a rotated HVFSR to evaluate directional resonance and determine the frequencies at which ground motion reaches maximum values in the horizontal. To do this, we first rotated the horizontal components of the pre-processed accelerogram at 10-degree intervals from 0 to 180 degrees at each station, and then we calculated each rotated HVFSR associated. Next, the resulting spectra were smoothed using a 20% Konno-Ohmachi window for improved visualization. Finally, we averaged the spectra and generated a representative curve for each azimuth, providing a simple function of frequency and movement. To take advantage of the arrangement of temporary stations installed, we estimated the standard spectral ratios (SSRs) to evaluate the relative amplifications among stations generated by the topographic conditions. For doing this, we used 10 s of S-wave in the SSRs calculation due to the improved results of Massa et al. (2014) (Massa et al., 2014) for this time window. Finally, we calculated the quotient among stations in the crest and stations in the base to identify amplification values at frequencies different from the fundamental one.

Although the rotated HVFSR helps to define horizontal polarization, the time domain method allows having a direct estimate of polarization angle. Therefore, we implemented the three components for estimating the ellipsoid polarization from eigenvalues and eigenvectors of the covariance matrix (Jurkevics, 1988). Before calculating, we filtered the signals between the frequencies where the rotated HVFSR reached the maximum values. Posteriorly, for each event, we estimated the covariance matrix running window with 0.5 s width and a 20 percent overlap (Pischiutta et al., 2012). To improve the results, we implemented the hierarchical criteria defined by Pischiutta et al. (2014) (Pischiutta et al., 2012, 2014). Then, we filtered the three parameters of the polarization ellipsoid: azimuth, rectilinearity, and apparent incident angle. A circular histogram of azimuth is plotted for rectilinearity values between 0.5 and 1 and values of incident angles between 45° and 90°.

3. Data implementation

Pereira City is widely recognized as the capital city of the coffee ground region in Colombia, making it an ideal candidate for studying the site and topographic effects. The geological and geomorphological context of the city has a complex topographic environment covered by soft-silty volcanic ashes with depths of up to 30 meters (Díaz et al., 2021; Universidad de los Andes – CARDER, 1999). Given the intricate soil structure and the city's significant size, Pereira has become a prime location for seismic microzonation studies, geophysical characterizations, and seismic instrumentation since the 90's. This section presents the dataset collected from various permanent and

temporary stations historically established throughout the city. We also outline the methodology and show our results for Pereira.

3.1 Strong motion data and location

We used two datasets of accelerometer recordings from both permanent and temporary stations (Fig. 1). The first dataset corresponds to the ground motion network in Pereira, which has varying historical records across stations. Specifically, data were available for the BATA station between 1995 and 2000, the MAZP and UTP stations from 1996 to 2011, and the CAST station from 1996 to 2010. In contrast, the Colombian Geological Survey (SGC in Spanish) has been operating CUBA and CBOCA since 2011, recording data from these stations. Additionally, the SGC installed three portable accelerometers (PERC1, PERC2, and PERC3) on the hillside between 2019 and 2021. These stations are located along the profile, where we found an evident difference between PERC1 and PERC3, with a 55-meter elevation difference between them and a slope reaching 40 degrees.

The local geology of Pereira is primarily characterized by Quaternary sedimentary deposits forming part of the Armenia fan, which overlie older, stiffer bedrock (Cretaceous rocks and Paleozoic schists) as described in Section 1. Within this geological framework, the stations are situated on different subsurface conditions. Most stations, including BATA, UTP, CUBA, PERC1, PERC2, and PERC3, are located on alluvial and fluvio-volcanic deposits, whose composition can vary from sands and gravels to volcanic ashes depending on their specific location. In contrast, the stations MAZP and CAST are situated on deep and old anthropogenic landfills, typically composed of fine materials, that cover the canalized canalized Egoyá stream. The CBOCA station, on the other hand, serves as our hard-rock reference site, located directly on the underlying bedrock. The variability in these subsoil materials across the network, ranging from hard rock to stiff soil deposits and landfills, influences the seismic response and is further characterized by the empirical site classification based on resonance periods from HVRSR curves derived from the accelerometric records, as discussed in Section 3.3.1.

We identified 96 earthquakes for our analysis after visual inspection of the records and the selection of signals with higher PGA values using a threshold value of 0.1 gals. Figure 2 shows the geographic distribution of the epicenters, with the deepest event being 160 km. Despite the M6.1 Eje Cafetero (Coffee zone) Earthquake in 1999 having reached a PGA of 292 gals at the MAZP station, nearly 80% of the recorded PGAs were less than 25 gals. The most significant events recorded in temporary stations were the Mw 5.1 La Victoria and Mw 6.1 Mesetas earthquakes, which reached PGAs of 29 and 20 gals, respectively.

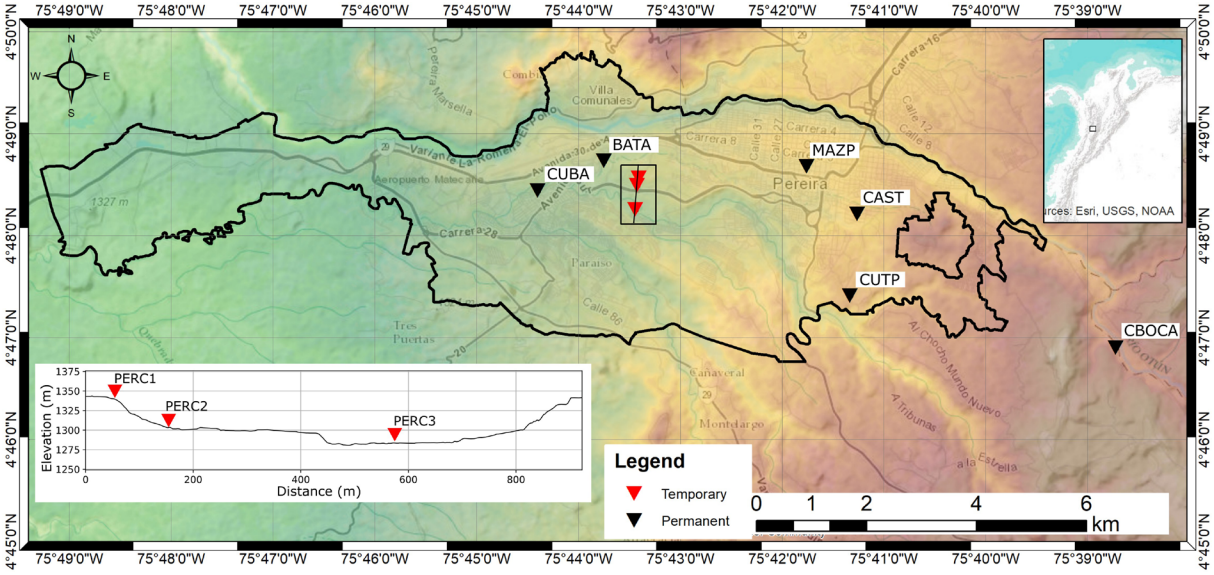

Figure 1. Location of the ground motion stations of Pereira used in this study. Black triangles represent permanent stations. Red triangles are temporary stations located along a profile to evaluate the topographic effect. Basemap colors are indicating the elevation.

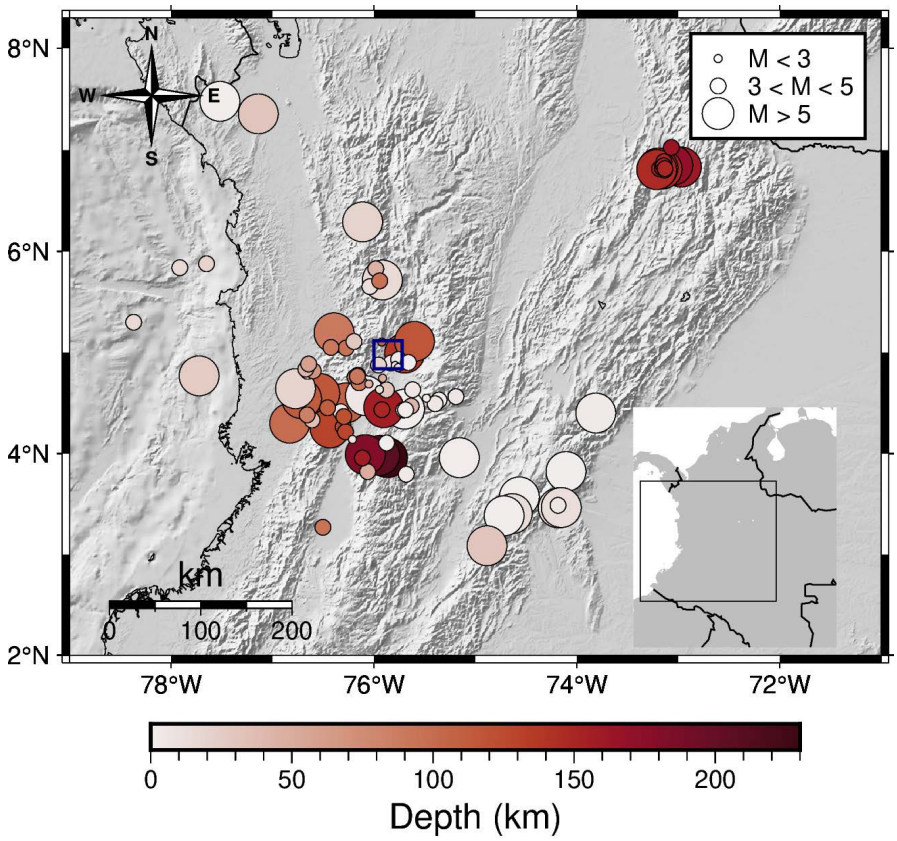

Figure 2. Seismicity distribution was recorded between 1996 and 2021 by temporary and permanent stations in Pereira. The colorbar indicates hypocenter depth, while the circle size depicts the local magnitude calculated by the SGC (Servicio Geológico Colombiano, 1993) (Servicio Geológico Colombiano, 1993). The dark blue square indicates the Pereira's location.

3.2 Additional data for validation

To achieve the primary objective of this study – developing a framework for site characterization using seismic records – it is crucial to include supplementary data for validating the proposed methodologies and results.

In the case of Pereira, two seismic zonation studies have been conducted. The first was completed in the late 1990s (Universidad de los Andes – CARDER, 1999), while the most recent study, undertaken in 2021, was a collaboration between the Colombian Geological Survey and the local risk management office at the Pereira City Hall. Both studies provided the city with a set of homogeneous seismic response zones, each characterized by amplification functions corresponding to various shaking levels and return periods. As these amplification functions and homogeneous zones were derived from detailed geophysical, geotechnical, and geological soil characterizations, this study utilizes both the raw geophysical data and the resulting amplification functions as benchmarks for validation. The validation approach is outlined below.

3.2.1 Geophysical information

The most recent soil characterization in Pereira was conducted using 158 V_s profiles and H/V Fourier spectra (HVFSRs). These data were distributed across urban and peri-urban areas, aligning with the seismic response zones defined in previous studies. This characterization followed the methodology described by (Mercado et al., 2023), employing triangular arrays to perform microtremor measurements using the SPAC methodology (Aki, 1957; Cho et al., 2004, 2013) and directly inverting the resulting dispersion curves (Pelekis and Athanasopoulos, 2011). Figure 3 illustrates the spatial distribution of this geophysical data in Pereira, highlighting that the characterization sites are in close proximity to the various seismic stations.

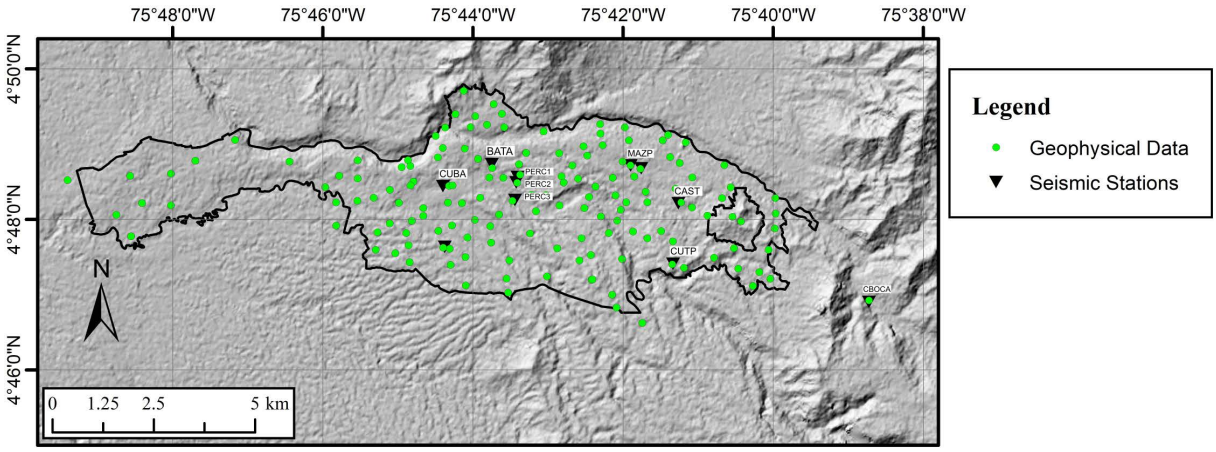

Figure 3. Spatial distribution of geophysical data from the seismic zonation study of the city. Adapted from Díaz et al. (2021).

Figure 4 shows the spatial distribution of the natural period (T_n) and Vs_{30}, based on the city's microzonation study. Figure 5 presents scatter plots illustrating the relationships between key soil parameters, including T_n, Vs_{30}, and predominant frequency, as well as the correlation between basin depth, Vs30, and natural frequency. The data indicate that, for Pereira, basin depth is proportional to both Vs_{30} and frequency. Furthermore, as expected, frequency and Vs_{30} exhibit a proportional relationship. To better illustrate the observed trends, Fig. 5 includes trend lines and the corresponding parameters from linear regressions applied to the data. Although the maximum R^2 values from the linear regression was always under 0.6, a general trend is observed.

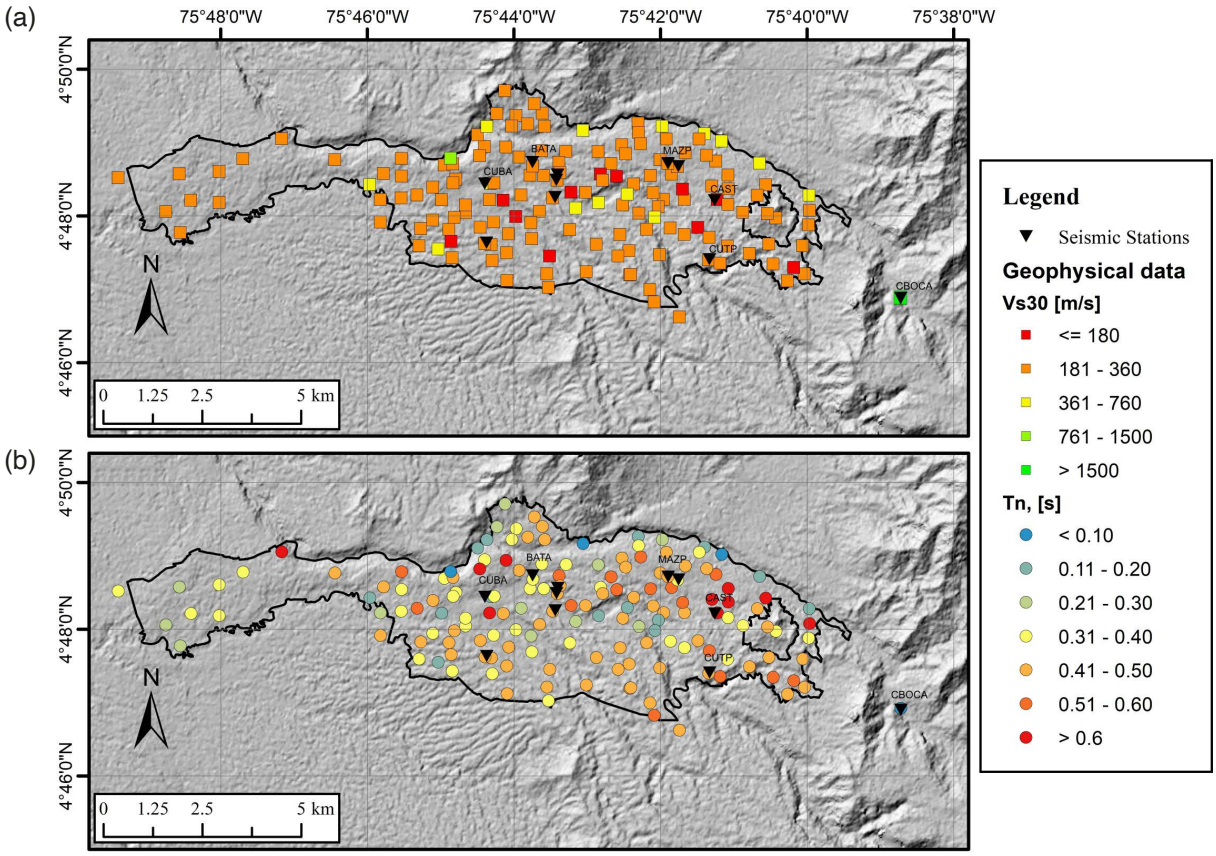

Figure 4. (a) Spatial distribution of Vs30 and (b) natural period from the geophysical characterization. Adapted from Díaz et al. (2021).

In this work, we used the H/V Fourier spectra from the microzonation studies to validate the results obtained with the proposed methodologies in the results section. More details about the geophysical characterization performed to the city from microtremor measurements can be found directly in the study performed by Díaz et al. (2021).

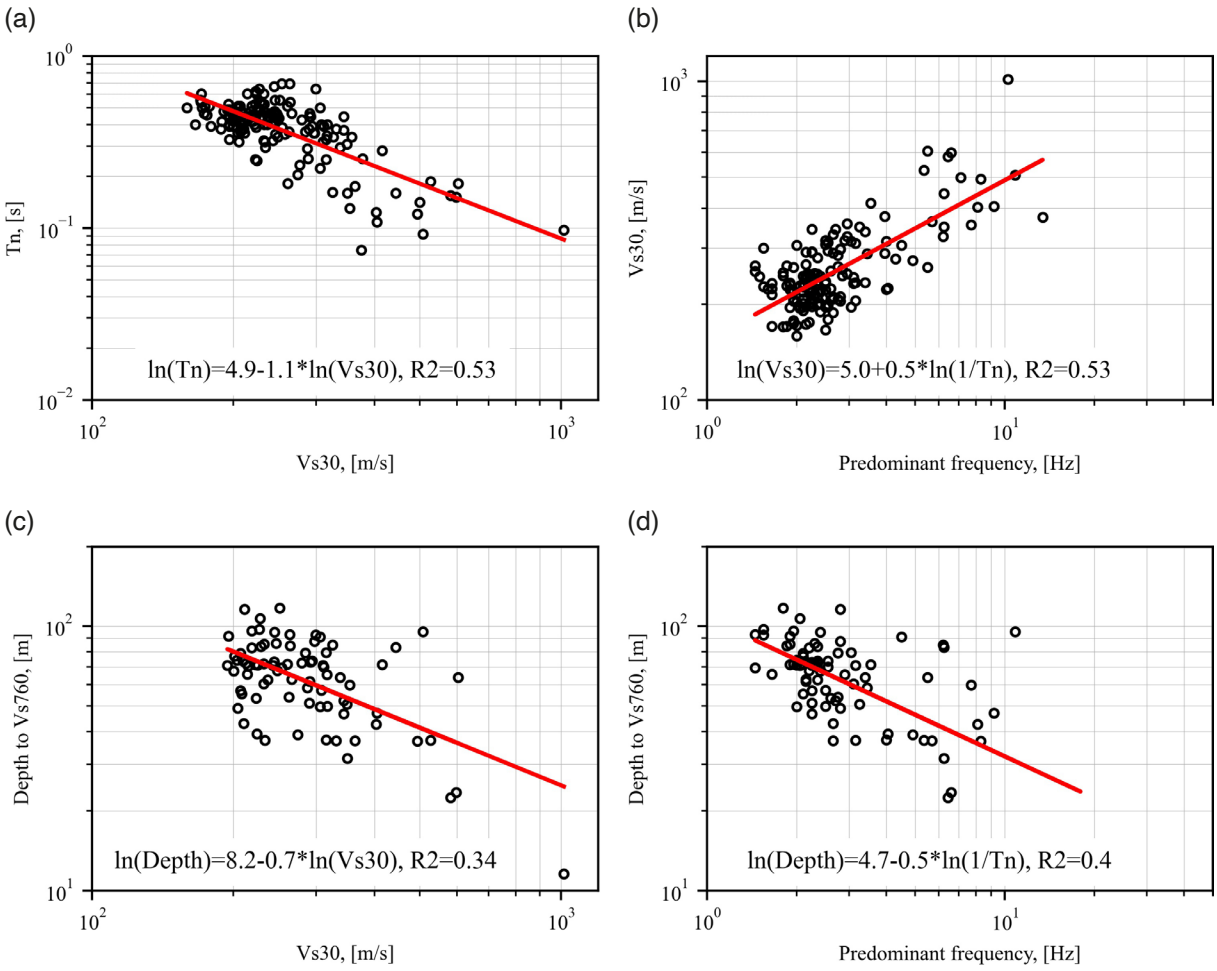

Figure 5. Scatter plots of soil parameters in Pereira soil deposits, (a) Vs30 vs natural period (Tn), (b) Vs30 vs natural frequency ($1/T_n$), (c) Depth to a layer with Vs value of 760 m/s vs Vs30, and (d) Depth to a layer with Vs value of 760 m/s vs natural frequency.

3.2.2 Amplification functions and seismic microzonation map

As mentioned before, the last seismic microzonation of the city was performed by Díaz et al. (2021). Briefly, the study used a comprehensive methodology to identify homogeneous amplification zones and to characterize the amplification functions (in term of spectral accelerations) to each zone. The study included the following main activities:

- Study of the historical seismicity of the city.
- Seismic hazard assessment at a rock condition.
- Processing and interpretation of ground motion seismic records from regional and local networks at the city (see previous Section 3.1).
- Construction of a geotechnical database.
- Geophysical characterization of the city (see previous Section 3.2.1).
- Construction of 1D models to perform non-linear site-response analysis of the soil, at 71 different sites where the best information was available.
- Validation of numerical models from seismic data recorded within the city.

– Estimation of amplification functions at four different PGA values for rock (0.04, 0.17, 0.25, and 0.48) at the different modelled sites.

The microzonation study included the 1D modelling of 71 sites using the software Deepsoil (Hashash et al., 2020). Figure 6 present the spatial distribution of the numerical models, and how almost all the sites with seismic stations were selected for this analysis. Given that most of the stations were included in the analysis, the seismic records obtained on them were used to validate the numerical models in the original study. As an example of the amplification functions estimated in the microzonation study, Fig. 7 presents the average amplification functions at the site of MAZP stations.

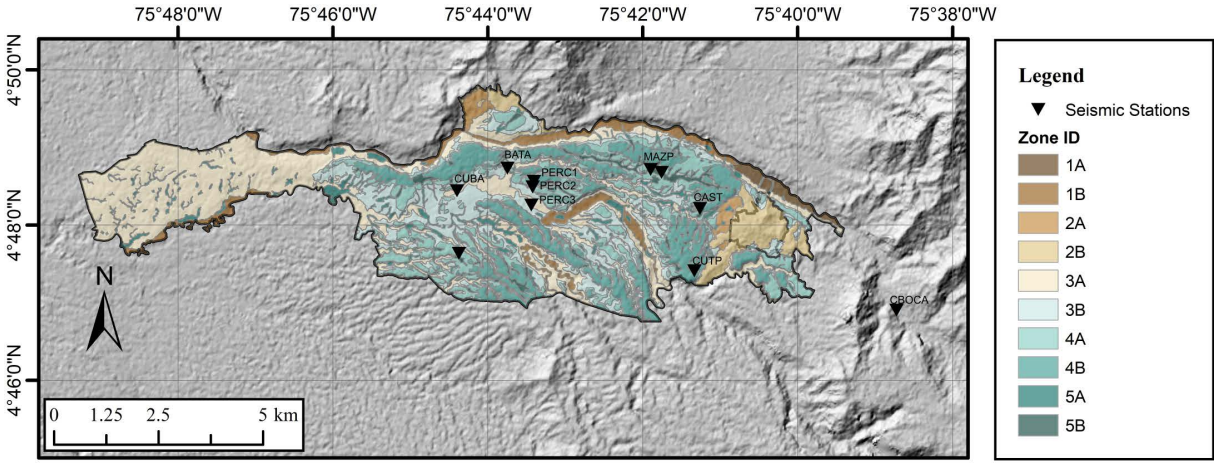

Figure 6. Spatial distribution of the 1D numerical models developed by Díaz et al. (2021).

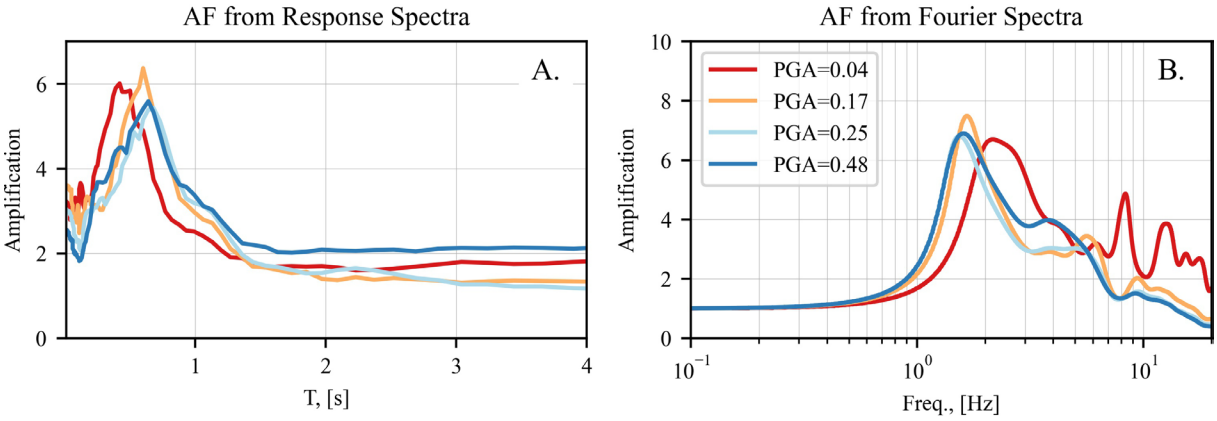

Figure 7. Amplification Functions estimated for MAZP. (a) In terms of response spectra, and (b) in terms of Fourier spectra.

After the 71 models were performed, 10 different seismic zones were defined from the aggrupation of sites with similar amplification functions and subsoils properties. The different zones lead to distinguish between alluvial deposits, residual materials, volcanic-ashes deposits, and deposits with important in-filled materials from anthropogenic origin. Figure 8 presents a figure with the spatial distribution of the different zones defined by the microzonation studies, while Fig. 9 for instance, presents the amplification functions at PGA, Sa (0.3 s) and Sa (1.0 s) in the different 10 defined zones.

In this work, we used specifically the amplification functions from 1D modelling at the lower intensity shaking in the specific site where the seismic stations are located to validate the empirical amplifications obtained in the results section of this paper (Table 2).

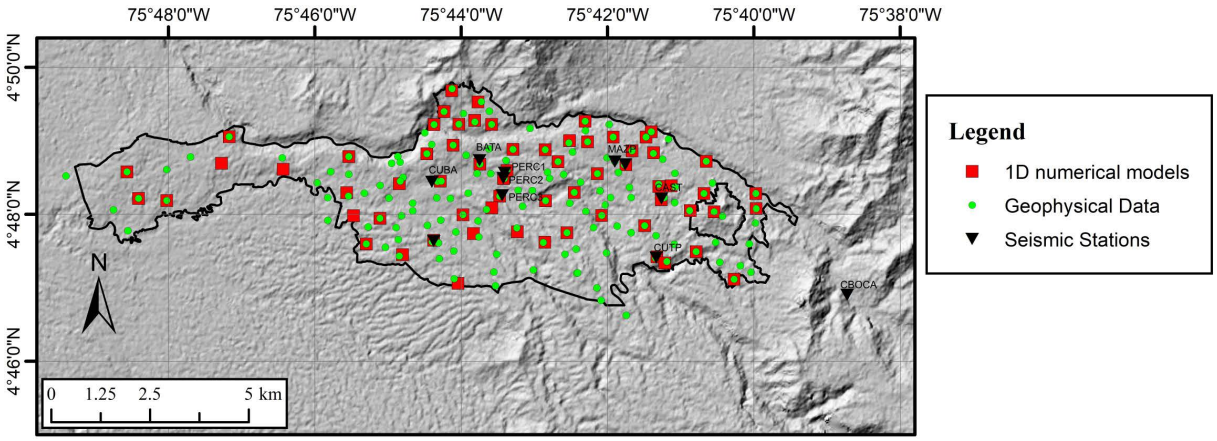

Figure 8. Microzonation study map for Pereira city. Adapted from Díaz et al. (2021).

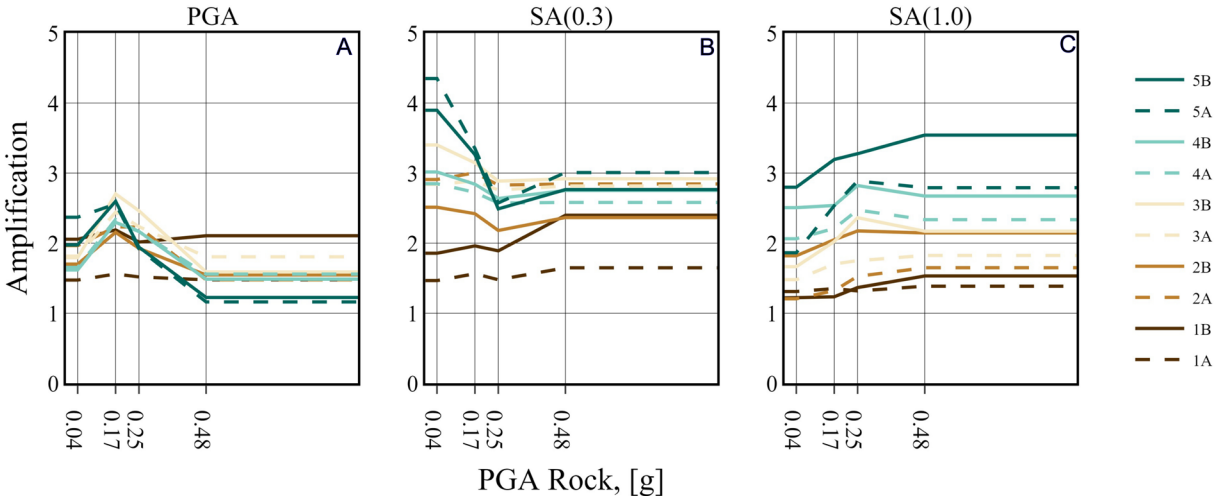

Figure 9. Amplification functions defined in the different seismic zones at PGA, Sa (0.3 s) and Sa (1.0 s) in terms of PGA value in rock level. Adapted from Díaz et al. (2021).

Table 2. Description of seismic zones. Adapted from Díaz et al. (2021).

ID	General description	Expected depth up to Vs of 360 m/s [m]	Range of depth up to Vs of 760 m/s [m]	Expected Vs30 [m/s]	Range of Tn [s]
1A	Conglomeratic materials and highly rigid clast-supported flows	<7	60-80	>450	<0.25
1B	Layers of sandy silty to sandy silty gravelly laharic flows up to 7 meters thick on highly rigid clast-supported flows	<7	40-90	250-600	0.1-0.3
2A	Silty sands resulting from the total weathering of the rock on a residual profile of rock	15-30	30-90	±300	0.2-0.5
2B		30-45	70-90	±250	0.4-0.7

ID	General description	Expected depth up to Vs of 360 m/s [m]	Range of depth up to Vs of 760 m/s [m]	Expected Vs30 [m/s]	Range of Tn [s]
3A	Sandy silt deposits of volcanic origin on top of sandy silts with low humidity and presence of gravels	<30	40-110	250-450	0.3-0.5
3B		<30	50-110	150-360	0.3-0.6
4A		30-40	60-110	150-300	0.4-0.7
4B		>40	70-110	150-300	0.4-0.7
5A	Sandy silt deposits of volcanic origin with presence of antropic in-fills on top of sandy silts with low humidity and presence of gravels	<30	30-130	±150	0.3-0.7
5B		>30	70-130	±150	0.4-0.7

Given the information from the latest microzonation study presented before, we assigned the Vs_{30} and natural period to the different stations from the geophysical characterization carried out in that study, and we assigned the corresponding seismic zonation study, a summary is presented in the Table 3. In the case of CBOCA station, it was located outside the microzonation study area, however it is located in a very stiff site with a Vs profile which reach up to 760 m/s at depths around 10 m.

Table 3. Geophysical properties estimated at the seismic stations from the geophysical characterization.

Station	Vs30 [m/s]	Tn [s]	Seismic zone
BATA	311	0.32	3A
CUBA	263	0.36	3B
MAZP	221	0.4	5A
CAST	171	0.61	5B
CUTP	219	0.45	4B
PERC1	208	0.48	4A
PERC2	189	0.42	4A
PERC3	247	0.43	3B

3.3 Results and discussion

3.3.1 Site classification

The classifications defined previously in Table 1 were obtained in regional studies; for local context, the geology and topography could have a crucial role in the seismic response (Posada et al., 2022). Due to this fact, we used a mix of Di Alessandro et al. (2012) and (Idini et al., 2017) classes to improve the characterization in Pereira. Table 4 shows the classification with the best adjustment to Pereira. We do not discriminate classes higher than 0.6 s because our sites do not reach up to 0.67 s. In general, the available earthquake ground motion records used for each station varies: BATA (4), CAST (9), CBOCA (9), CUBA (16), PERC1 (40), PERC2 (25), PERC3 (47), MAZP (27), and UTP (24).

Table 4. Classes implemented for Pereira. We used a combination of categories by Idini et al. (2017) and Di Alessandro et al. (2012). P* indicates the amplitude of H/V curve.

Site class	Description	Classes for P*	P*
CL-I	$T \leq 0.2$ s	A	$2 \leq P^* < 3$
CL-II	$0.2 \text{ s} \geq T < 0.4$ s	B	$3 \leq P^* < 4$
CL-III	$0.4 \text{ s} \leq T < 0.6$ s	C	$P^* \geq 4$
CL-IV	$T \geq 0.6$ s		
CL-V	Not identificable (flat HVRSR and amplitude <2)		

Based on Table 4 and similar to Di Alessandro et al. (2012), the first class (*CL-I*) defines hard soil with periods of less than 0.2 s. The second class (*CL-II*) is associated with intermediate stiffness soils and natural periods between 0.2 and 0.4 s. The third class (*CL-III*), defined by periods between 0.4 and 0.6 s, represents intermediate-soft stiffness soils. Finally, the fourth class (*CL-IV*) has periods larger than 0.6 s, allowing associate soft soils. In the same way, to improve site classes for Pereria, adding the P* from Idini et al. (2017) as a weight to the amplitude HVRSR. This classification is also like the one defined by Mercado et al. (2023) for the soils of Northern South America, who described an additional break for natural periods over 0.8 s.

After obtaining the Natural period through the HVRSR curves, we classified the sites according to Table 4. We identified five classes in Pereira: *CL-V*: CBOCA station, *CL-IIB*, PERC2 station, *CL-IIC*: BATA and CUBA stations, *CL-IIIC*: PERC1, PERC3, and UTP stations, and *CL-IVC*: UTP and CCAST stations. This classification allows us to identify the CBOCA station as a hard-rock site, defined in this study as a reference site for relative amplification calculations. The significance of P* is demonstrated by comparing BATA, CUBA, and PERC2 stations, which are in the same period cluster, according to Di Alessandro et al. (2012). However, PERC2 has lower amplitudes than the other stations, probably because of the topographic effect due to its location on the base of the hill (Massa et al., 2014) or potentially due to local soil conditions and stratigraphy influenced by its position (Fig. 10a). Finally, the MAZP and CCAST stations are located over Pereira's softest soils, with periods of 0.63 and 0.67 s, respectively (Fig. 10b).

The variations of our empirical site classification depend essentially on the thickness of the soils and modifications generated by the topography. We noted how the local geology modified the seismic response among the sites, particularly in the landfills, where periods and HVRSR amplitudes increase associated with MAZP and CCAST stations (CL-IVC). Instead, differences between CL-IIIC, CL-IIC, and CL-IIC classes are associated with the soil rigidity and the thickness of the soils (Díaz et al., 2021). Based on the empirical site classification (Table 4) and the geological description of the station locations, our results indicate a broad consistency between the defined site classes and the general geological context (hard rock, alluvial/fluvio-volcanic deposits, landfills) of the study area; however, this is not a rule for places with more complex geological settings (Chopra et al., 2018; Posada et al., 2022).

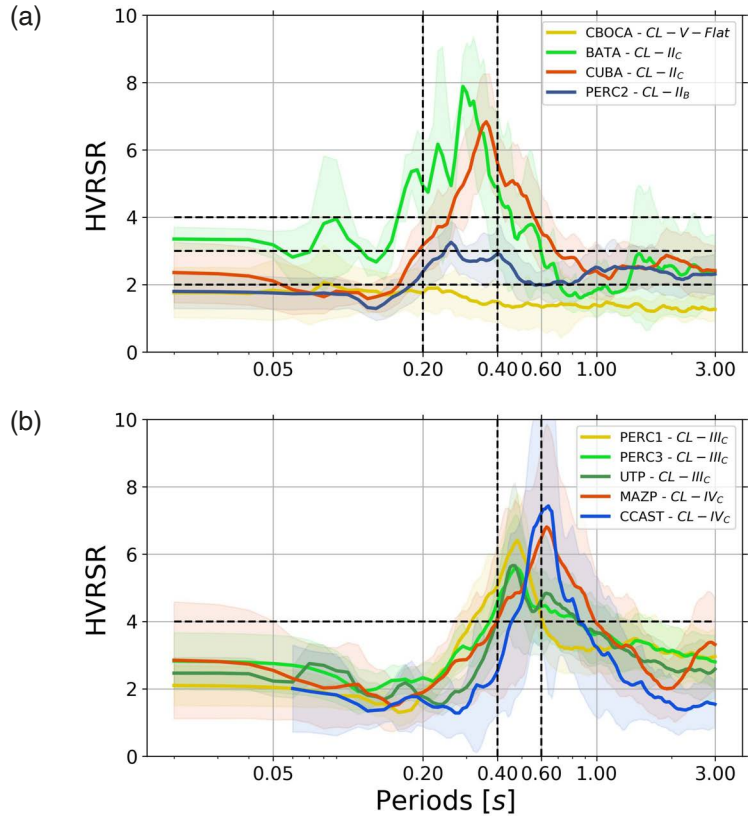

Figure 10. Averaged spectral ratios (HVRSR) with their standard deviation and site classes for Pereira. (a) BATA and CPER stations correspond to the CL-IIC class. The PERC2 station corresponds to the CL-IIB class. The CBOCA station has a flat curve associated with hard-rock (CL-V). (b) PERC1 and PERC3 stations correspond to the CL-IIIc class, and MAZP and CCAST stations to the CL-IVC class.

The topography can be a critical factor in the seismic response and has a crucial role in Pereira; a clear example is the PERC2 station, located on the base of a hill, which shows a significant reduction in the HVRSR amplitude related to the deamplification. This phenomenon has been analyzed in Italy through local instrumentation (Massa et al., 2014). Directly, the HVRSR curves do not always reach to show the amplification alterations product of the topography. Such is the case of the PERC1 station, which, despite its location, does not present irregular amplitude values.

Additionally, we generated representative HVRSR curves for each class by averaging the individual curves within each group. Afterward, we calculated the relative amplification for each site by dividing the HVRSR curve by the reference site (CL-V class). Figure 11a shows amplifications below values of 2 for the CL-IIB, indicating relatively low amplification. In contrast, the CL-IIC and CL-IIIC classes have amplification values ranging from 4 to 5. The CL-IVC class exhibits the highest amplification value of 5.4, as shown in Fig. 11d. To evaluate the reliability of these relative increases, we compare them to the 1D nonlinear amplification model computed for the microseismic zonation of Pereira (Díaz et al., 2021). Comparing the relative amplification calculated for the defined soil classes (empirical curves, shown in blue) with the predictions from the 1D amplification models (red curves) in Fig. 11, we observe that the 1D approach provides a reasonable general estimation for some classes and frequency ranges. However, significant discrepancies are apparent for certain classes, most notably for CL-IIB (Fig. 11a), which is represented by the PERC2 station. The substantial difference observed here between the empirical amplification and the 1D model is primarily attributed to the influence of complex local topography at the PERC2 site. PERC2 is situated at the base of a prominent hill (see Fig. 1 for station location), a setting where seismic wave propagation is significantly modified by 2D and 3D topographic effects or by the stratigraphy. Unlike 1D numerical models that assume horizontal layering and vertical wave propagation, these effects, such as de-amplification at the base of slopes or amplification at hilltops, are not accurately captured by 1D models. The empirical curve for PERC2 in Fig. 11a reflects the actual site response including this topographic influence, while the 1D model, based on

a simplified vertical soil profile, does not. This discrepancy underscores the limitations of 1D models in complex terrains and highlights the critical importance of considering topographic effects for accurate seismic response assessment. Furthermore, the difference observed between the relative amplification for CL-IVC (Fig. 11d) and the 1D model is primarily associated with the model's limitation in accurately representing the complex dynamic behavior of landfills.

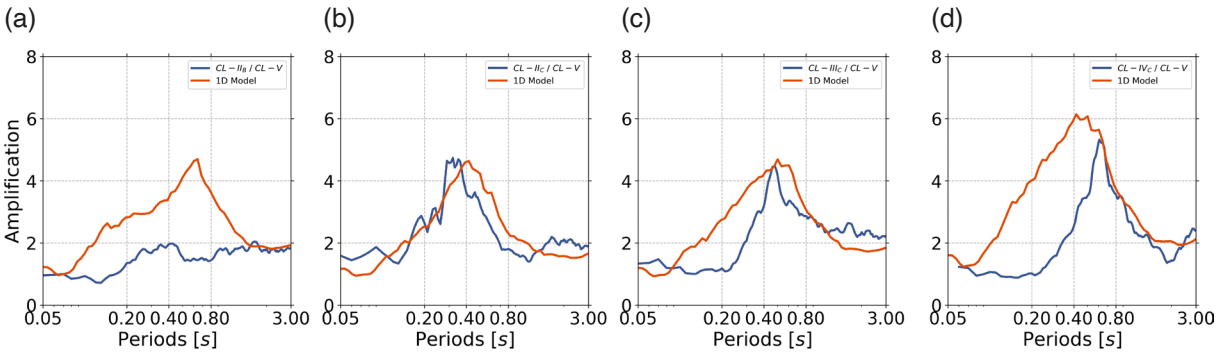

Figure 11. Relative amplification (blue line) concerning CL-V (hard rock) for each class. The periods of maximum amplifications are close to the natural periods. The red line corresponds to the 1D amplification model associated with each class (Díaz-Parra et al., 2021). (a) CL-IIB. (b) CL-IIC. (c) CL-IIIC. (d) CL-IVC.

3.3.2 Index K_g

Although the empirical base of this method is developed from ambient noise data, we implemented earthquake signals to build the HVFSRs and compare them with the K_g values obtained from microtremor measurements. Microtremor data are from circular arrays taken for the seismic response zonation study (Díaz et al., 2021). To relate these measurements, we tried to ensure the same local conditions using the nearer microtremor circular array to each station; however, this is not possible in some places due to the topography or a suitable location around the station.

As a result, the HVFSR curves obtained from earthquake data and ambient noise data show reasonable agreement in terms of peak frequency and shape for the CCAST, PERC3, and CUBA stations. While not a perfect fit due to the inherent differences in the wavefields and data characteristics, the overall trends are similar. However, significant discrepancies were observed when comparing the earthquake and microtremor HVFSRs for the MAZP, UTP, PERC1, and PERC2 stations. The reasons for these differences vary by station and highlight the sensitivity of HVFSR to specific local conditions and measurement locations:

- For MAZP, a notable difference in peak frequency and curve shape is observed (Fig. 12b). This discrepancy is primarily attributed to a logistical factor: due to the original permanent station having been retired and its site subsequently occupied by a new building, the microtremor measurements for MAZP had to be conducted at a slightly different location. This change in measurement point likely reflects varying local soil conditions, which consequently influenced the observed seismic response. This minor spatial separation, combined with potentially high spatial variability of subsoil properties characteristic of anthropogenic landfill materials at this site, likely contributed to the observed difference in response characteristics between the two measurement points.
- For PERC1 and PERC2, discrepancies are also evident when comparing their earthquake and microtremor HVFSRs (Figs. 12e and 12f). Similar to MAZP's situation but related to terrain challenges, the microtremor measurement locations from the microzonation study were not performed at the exact same spot as the permanent stations due to difficult topographic conditions (PERC1 on a hilltop, PERC2 at the base of a hill). Local subsurface variations and small differences in measurement points in these complex topographic settings can lead to differing seismic responses.
- For the UTP station (Fig. 12c), a particular situation occurs where despite the permanent station and microtremor measurement sites being located nearby and on the same general geological material, the HVFSR curves do not show a close fit. This suggests the influence of local heterogeneities or other uncharacterized site conditions at a very localized scale, affecting the response differently for earthquake and noise wavefields at these specific points.

Beyond these site-specific discrepancies or agreements, it is important to note general factors influencing the comparison between earthquake and ambient noise HVSRs. While the fundamental frequency estimation might show stability across methods for certain sites (e.g., UTP, CUBA, PERC1, and PERC3 to varying degrees), variations in the amplitude peaks are common. The two methods inherently use different data sources (earthquake vs. ambient noise), and additional uncertainties are associated with the results, particularly regarding amplitude. Factors such as seasonal local wind and temperature conditions can significantly affect noise H/V amplitudes over frequency ranges between 2-18 Hz (Hillers and Ben-Zion, 2011), influencing apparent amplification in both soil and rock site classifications (Cara et al., 2003). Furthermore, the level of anthropogenic noise, sometimes related to the hour of the day when records are acquired (Benkaci et al., 2021), can also affect the H/V amplitude, with some studies reporting changes up to 37% over the peak amplitude associated with this effect (Volant et al., 1998). These factors contribute to the observed variability in amplitude peaks when comparing noise and earthquake-based site response estimates.

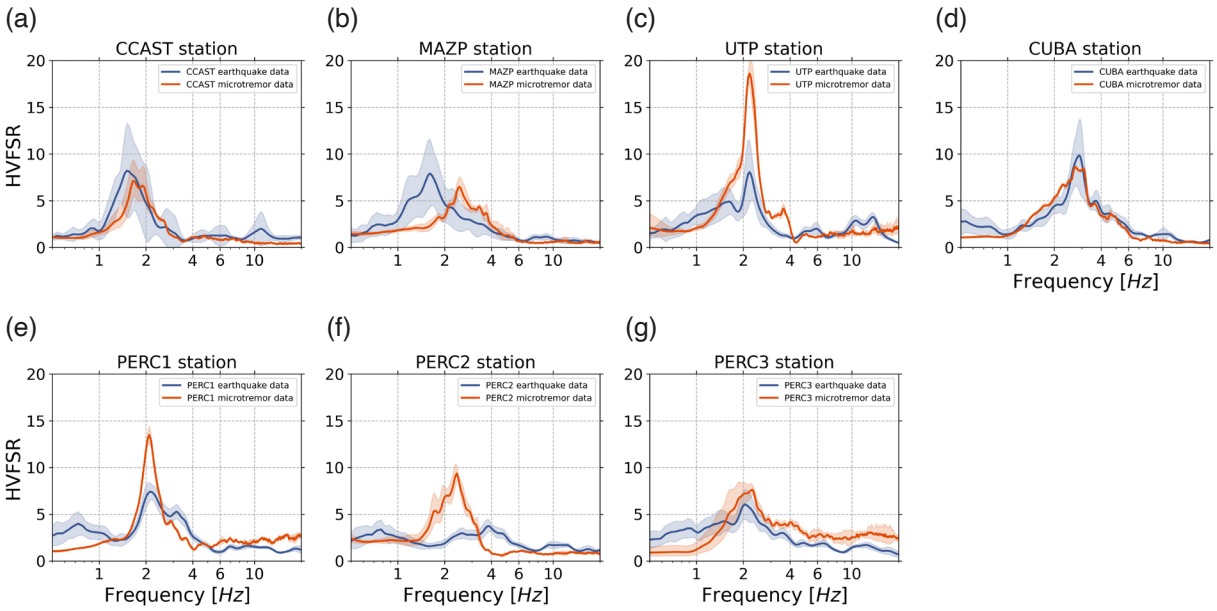

Figure 12. Averaged Fourier spectral ratios (HVFSR) with their standard deviation calculated from earthquake data for Pereira (blue line) and HVFSRs calculated from microtremor data (red line). (a) The CCAST station. (b) The MAZP station. (c) The UTP station. (d) The CUBA station. (e) The PERC1. (f) The PERC2 station. (g) The PERC3 station.

Once the HVFSR curves have been obtained, we apply Equation 2 to calculate the K_g index at each station. Table 5 shows amplitudes, resonance frequencies, and K_g values for earthquake and noise data, which reflects the observed in Fig. 10. We do not have significant frequency changes at most stations, only at MAZP and PERC2, where the differences reach 1.1 and 1.5 Hz, respectively. The main variations are in the amplitudes, which are similar only at sites where the topographic effect is absent and the SPAC measure is nearby (CCAST, PERC3, and CUBA). Furthermore, at these sites, Kg index results do not exceed a variation of 40%, as Fig. 13 shows. Significative variations ranging from 79% to 165% of the Kg index are on complex topographic conditions; as expected, the UTP site represents the higher variation (Fig. 13). The meaningful changes could result from regional topographic conditions, where the surface waves of the ambient noise did not reach to record, and the ground motion waves did.

We found how the topography modified the seismic response knowledge; therefore, ground motion records are crucial in urban cities. This parameter allows us to estimate the empirical factor accurately to realize better the damage potential, liquefaction, and soil stiffness (Kang et al., 2022; Nakamura, 2019; Pamuk et al., 2018).

Table 5. Kg index results for earthquake and microseismic data. Differences are noticeable at sites where topography does not allow measurement.

Site	Earthquake Analysis			Microtremor analysis		
	Amplitude	Frequency	K_g	Amplitude	Frequency	K_g
UTP	8.1	2.1	31.2	18.6	2.2	157.2
MAZP	7.9	1.6	39.0	6.5	2.5	16.9
CUBA	9.8	2.8	34.3	8.6	2.7	27.3
PERC1	7.4	2.1	26.1	13.4	2.1	85.5
PERC2	3.7	3.8	3.6	9.3	2.3	37.6
PERC3	6.0	2.1	17.1	7.6	2.3	25.1
CAST	8.2	1.6	44.8	7.1	1.6	31.5

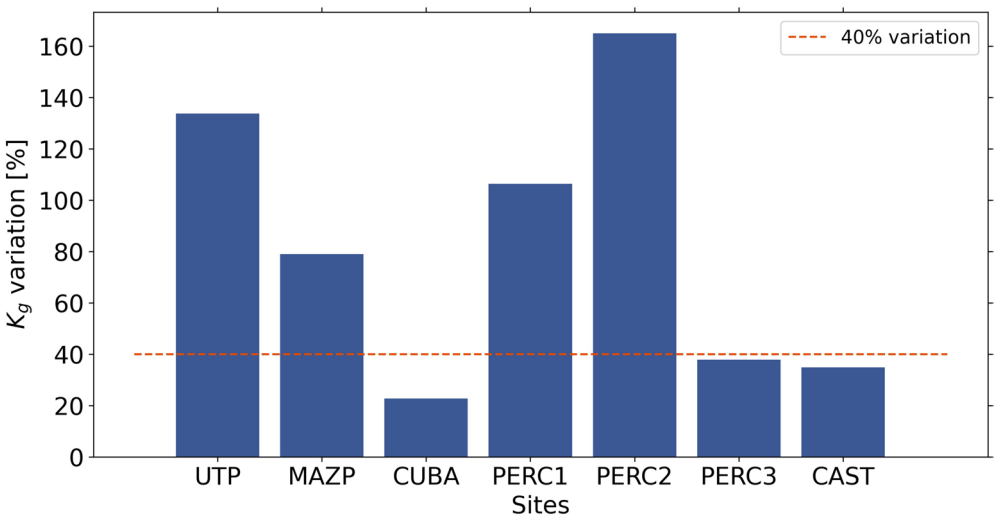

Figure 13. K_g index variation between earthquake and microtremor data. Stations with better adjustment are lower than 40%.

3.3.3 The empirical transfer function (ETF)

We identified the two higher earthquakes recorded in temporary and CBOC stations for calculating the response spectra, which are intraplate and crustal events associated with Mw 5.1 La Victoria and Mw 6.1 Mesetas, respectively. Then, we found the empirical amplification through the quotient between horizontal components of the PERC1, PERC2, and PERC3 sites and the CBOC site. Figure 14 shows our calculation; panels A and B are La Victoria records, while Panels C and D are from the Mesetas earthquake. PERC1 shows higher amplifications over the different earthquakes and components. Meanwhile, the north-south component denotes the difference between PERC2 and PERC3 sites. These amplification differences are the consequences of the station array configuration, wherein the topography modifies the records (see Fig. 1) or even the stratigraphy at the sites.

Variations in amplification ought to be linked with topography, as the proximity between stations and slight geological differences need not result in abrupt changes. We also observed that the La Victoria earthquake generates

amplifications above 10 in long periods at PERC1, which could be the topographic effect associated with the regional geomorphology, where the frequencies or wavelengths are related to the hill dimension (Pischiutta et al., 2022). ETFs are helpful inputs to the calibration process during the creation of 1D and 2D models, especially in 2D, where simulations can represent the topography.

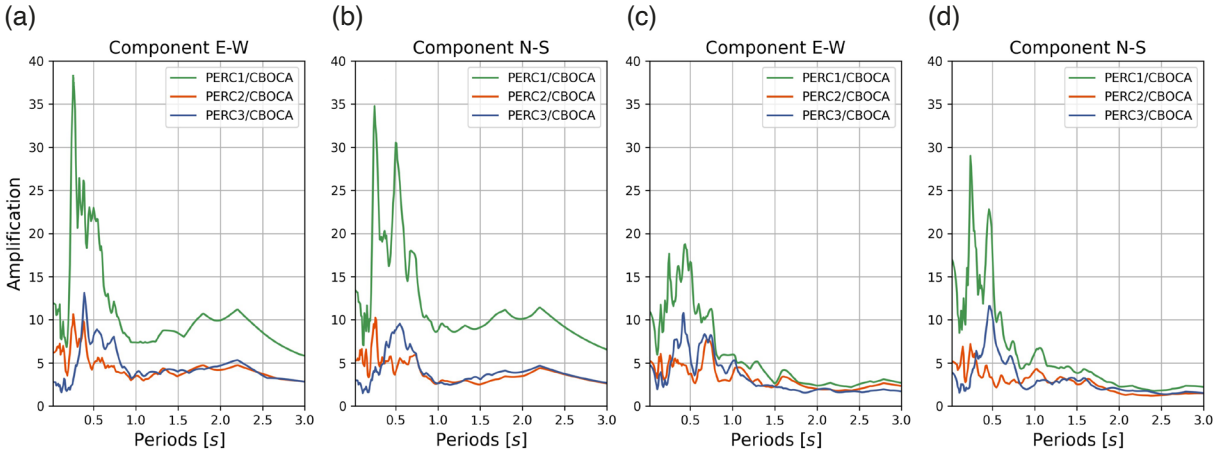

Figure 14. Empirical transfer functions (ETF) were calculated for two earthquakes. (a) and (b) correspond to the 5.5 Mw La Victoria event, and (c) and (d) correspond to the 6.1M Mesetas event.

3.3.4 Terrain directional movement

We analyzed earthquake and noise data recorded to assess topographic effects on temporary stations. To calculate the noise HVFSR, we used 120 minutes of records and applied 60-second time windows. Then, we rotated and calculated each spectral ratio based on the guidelines outlined in SESAME (SESAME, 2004) using Geopsy software (Wathelet et al., 2020). Figure 15 summarizes the results of our earthquake and noise data analysis. The results generally show similar patterns between the two data types. However, at the PERC1 station, earthquake data shows higher amplitudes than noise data at the natural frequency (~2 Hz) and frequencies below 1 Hz, while noise data shows higher amplitudes between 2.5 and 3.5 Hz. At PERC2 and PERC3, the differences between the earthquake and noise data are despicable, but noise data provides a more straightforward definition of the natural frequency. Finally, we observed at PERC3 that the noise H/V amplitude is higher than the earthquake data. The variations between noise (or microtremor) and Earthquake data at the same sites have been studied and even corrected (Kawase et al., 2019). However, the azimuths display a similar pattern in both data, where the amplitude values match. These directions are associated with a directional amplification generated by the topography.

Based on previous studies, we know three main premises about the seismic response and topography. 1) Sites on the top ridges have higher amplifications, 2) Sites on the base have a deamplification effect, and 3) sites on flat places, the seismic response is not modified (Massa et al., 2014). Figure 1 shows a profile view of topographic conditions for the temporary stations, where PERC1 and PERC2 are at the crest and base of the hill, respectively. The topographic effect could modify the seismic response, generating a directional resonance along the axis of the steepest slope (Massa et al., 2014; Panzera et al., 2014; Pischiutta et al., 2012). PERC1 presents this phenomenon, where the main slope direction is oriented N10-20W. This preferred orientation of the topography is clearly reflected in the directionality of the seismic response identified through our analyses. Specifically, the Rotated HVFSR results (Figs. 15a and 15d) show maximum amplification values along azimuths centered around N10-20W (Azimuth 160° – 170°). These directional analysis methods, detailed in Section 2.4, thus allowed us to identify the consistency between the topographic orientation and the preferred direction of ground motion at PERC1. Otherwise, the PERC2 station on the steepest slope presents a deamplification coherent with the previous premises. Based on Fig. 1, PERC3 is situated in a small basin surrounded by hills and unaffected by topography like PERC1 and possibly PERC2. However, we observed variations in the amplitude of the rotated HVFSR at this site. Although we avoid exploring the basin effect in this study, these variations could be related to the geometry of the basin.

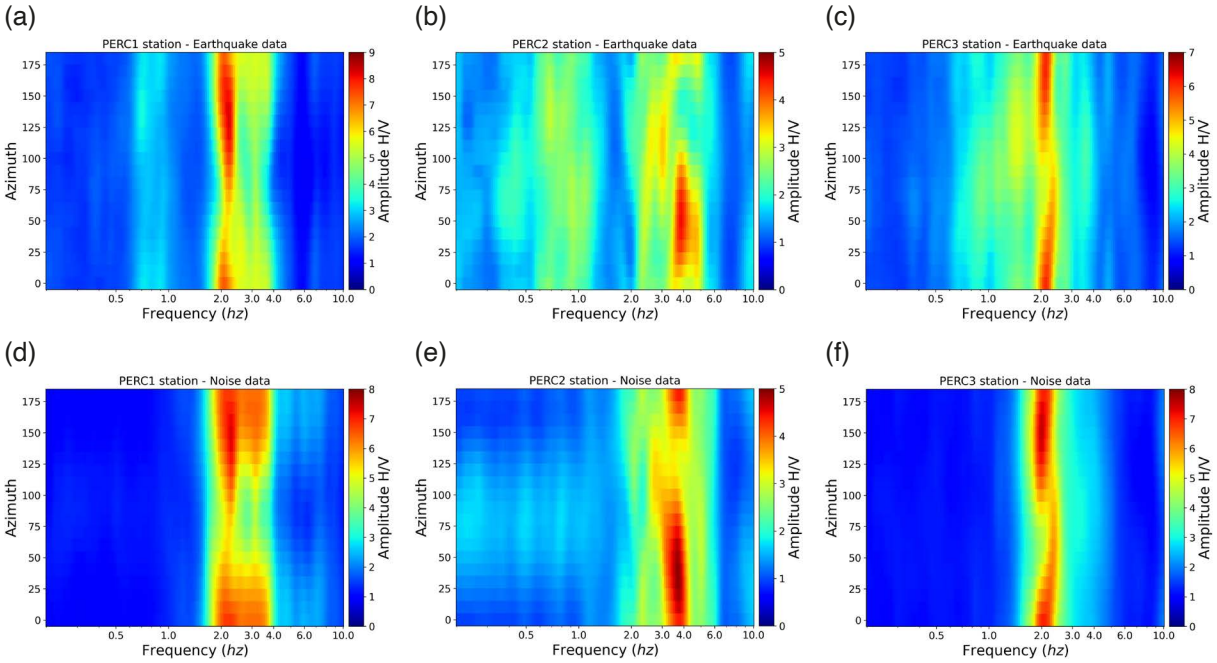

Figure 15. Rotated HVFSR for earthquake and noise data at temporary stations. (a) HVFSR calculated at PERC1 station using earthquake data. (b) HVFSR calculated at PERC2 station using earthquake data. (c) HVFSR calculated at PERC3 station using earthquake data. (d) HVFSR calculated at PERC1 station using noise data. (e) HVFSR calculated at PERC2 station using noise data. (f) HVFSR calculated at PERC3 station using noise data.

Similarly, we calculated the rotated HVFSR for three permanent stations (Fig. 16). Although the UPT station is near a small hill, the rotated HVFSR does not present significant variations along the evaluated azimuths (Fig. 16a). In contrast, MAZP and CPER stations are directly affected by topography. The First one is on an N5W (Azimuth 185°) moderate slope, coherent with the higher amplitude values at azimuths close to the slope direction (Fig. 11b). The location of the CUBA station presents flat topography but is limited by a scarp toward the northwestern. Figure 16c shows azimuths in an N30W (Azimuth 150°) direction, with higher amplitude values than in other directions.

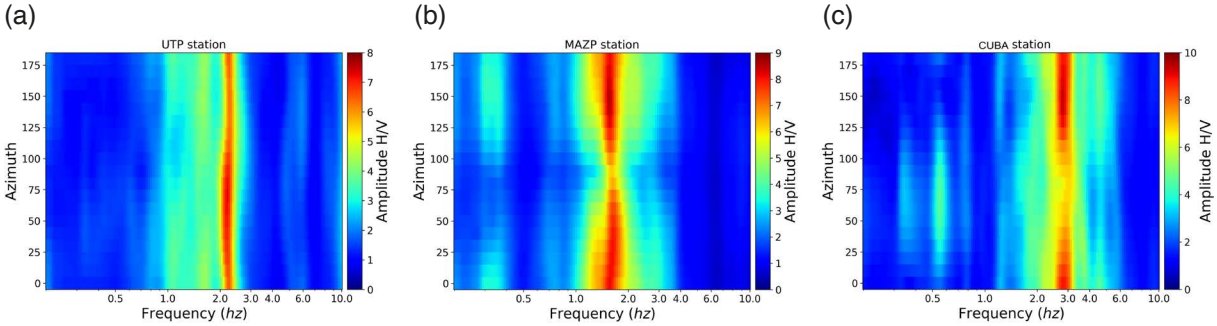

Figure 16. Rotated HVFSR calculated at permanent stations. (a) HVFSR calculated at UTP station using earthquake data. (b) HVFSR calculated at MAZP station using earthquake data. (c) HVFSR calculated at CUBA station using earthquake data.

Based on SSR calculation, we estimated amplifications among PERC1 y PERC2 sites concerning the PERC3 station. Figure 17a shows the first analysis between PERC2 and PERC3, which yields deamplification at 3.5 Hz or lower; nevertheless, from the frequency mentioned, the amplification reaches its maximum values between 10 and 20 Hz. Regarding azimuths, amplifications are associated with an orthogonal direction to the main slope between 50° and

70°. On the other hand, Figs. 17b and 17c show the amplifications calculated for the PERC1 station. Amplifications concerning PERC3 do not indicate significant values in the predominant frequency (2.1 Hz in Table 5), but at 4 and 7.5 Hz, we found values of 3.5 and 3.2, respectively. Although we have two top amplification picks, the azimuth directions vary between them, being 4 Hz in the main slope direction (170°) and 7.5 Hz in the orthogonal direction (60°-70°). Finally, Amplifications regarding PERC2 show two picks, the first at 2.1 Hz; this value does not correspond with the topography because this frequency coincides with the deamplification at PERC2 and the predominant frequency at PERC1. However, we can observe at 4 Hz an amplification that can reach up to 3.5 in the main slope direction (170°).

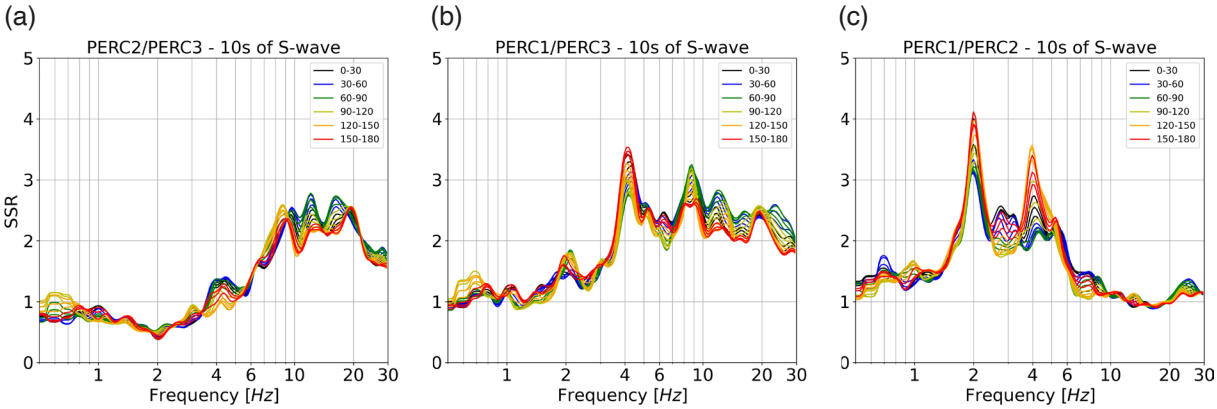

Figure 17. Rotated SSR calculated at temporary stations. (a) Rotated SSR between PERC2 and PERC3 stations. (b) Rotated SSR between PERC1 and PERC3. (c) Rotated SSR between PERC1 and PERC2.

To visualize and analyze the directional characteristics of ground motion, we applied polarization analysis, with results displayed on a 3D hill shade map in Fig. 18. By analyzing the polar histograms of polarization azimuth derived from earthquake data, we can identify the dominant directions of particle motion at each station, which are often related to directional resonance or scattering caused by local site conditions and topography.

Figure 18a presents the polar histograms for the temporary stations. The results for PERC1, PERC2, and PERC3 are shown in this panel, clearly labeled to distinguish each station's histogram. For PERC1, the polar histogram shows a precise concentration of polarization azimuths around N10W, consistent with the orientation of the main slope at the site and in agreement with the direction of maximum amplification observed in the rotated HVFSR analysis (Fig. 15). For PERC2, located at the base of a significant slope, the analysis also indicates a predominant directionality, centered around S80W (Fig. 18a). Note that polarization analysis primarily reveals direction of motion, not amplification/de-amplification magnitude, which is captured by spectral ratios (e.g., Fig. 15). PERC3, located on a flatter part of the profile, does not display a single, strongly concentrated polarization direction; instead, a broader distribution is observed with some trends around N10W and N50W (Fig. 18a). This pattern for PERC3 may be related to the local geology and hills surrounding the site, potentially indicative of complex wave scattering or trapping effects that prevent a single clear direction from dominating the earthquake wavefield polarization.

Other stations, including permanent stations, show varying polarization patterns. In the case of the UTP station (Fig. 18b), the polarization analysis indicates a predominant directionality around N60E. This result is notably different from the direction of maximum amplification observed in the rotated HVFSR analysis for UTP (Fig. 16a). Although UTP is located on moderate topography, the polarization pattern appears to reflect directionality potentially influenced by nearby scarps or small hills toward the southwestern and northeastern.

For the MAZP station (Fig. 18c), located on a heterogeneous landfill site, the polarization histogram shows a more scattered and less defined distribution of azimuths compared to other sites. This is likely a consequence of the complex internal structure and variability within the landfill material, which can cause significant scattering of earthquake waves and prevent a single dominant direction of particle motion from emerging clearly across the analyzed records. While the reviewer noted a potential influence of ambient noise on these data, this polarization analysis was performed using earthquake data as stated. The scattered pattern at MAZP is attributed primarily to the complex site structure influencing earthquake wave propagation directions.

For the CUBA station (Fig. 18d), situated near a scarp, the polarization analysis reveals a clear dominant directionality around N30W. This result is consistent with the orientation of the nearby scarp or geological boundary and aligns with the direction of maximum amplification observed in the rotated HVFSR (Fig. 16). While the reviewer noted a potential influence of ambient noise, the observed polarization pattern from earthquake data at CUBA reflects the influence of this site-specific structural feature on the direction of earthquake ground motion.

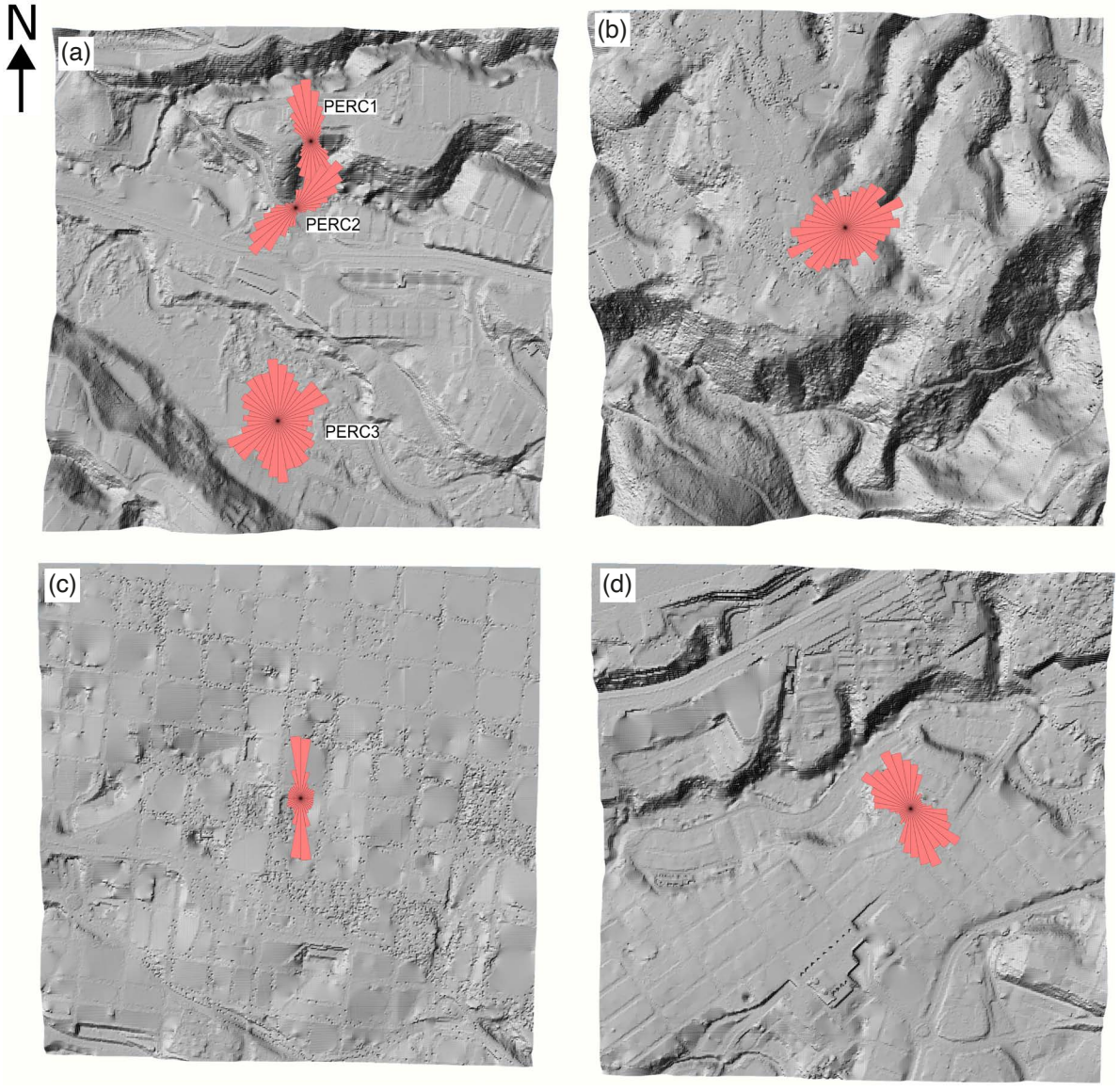

Figure 18. Polarization diagrams were obtained through the covariance matrix method. 3D Hillshade generated from a DTM (3 × 3 m) allows visualization of the excellent relationship between the topography and diagrams. (a) PERC1, PERC2 and PERC3 stations. (b) UTP station. (c) MAZP station. (d) CUBA station.

4. Conclusions

Our empirical site classification for Pereira stations was defined using a combination of the classes proposed by Idini et al. (2017) and Di Alessandro et al. (2012), which provided improved resolution for periods between 0.4 and 0.7 seconds. The differences observed across the five defined classes primarily depend on deposit thickness and modifications induced by topography. Local geology influenced the seismic response at sites underlain by anthropogenic fills, as observed at the MAZP and CCAST stations, which exhibited the highest natural periods and amplification values. As expected from seismic response fundamentals, sites on stiff soils or hard rock showed

lower fundamental periods, although topographic amplification was evident in some cases. Relative amplification with respect to the hard-rock reference site showed good agreement in areas with minimal topographic complexity, supporting its use as a proxy for 1D model estimation.

Originally designed for microtremor analysis, the Kg index was evaluated using earthquake records, yielding consistent results at stations such as CCAST, CUBA, and PERC3, where topographic influence is limited and microtremor measurements were taken nearby. In contrast, topographic constraints at PERC1 and PERC2 led to significant discrepancies due to the need for distant measurements. At MAZP, the variation was attributed to the heterogeneity of landfill thickness, and at UTP, topographic effects not evident in the microtremor data caused discrepancies despite the proximity of the measurement sites. In general, differences in Kg values remained below 40% for sites without major topographic influence but increased markedly in more complex terrains.

Two significant events (Mw 5.1 La Victoria and Mw 6.1 Mesetas) were used to compute empirical transfer functions (ETF) for the PERC1, PERC2, and PERC3 stations with respect to the CBOC reference site. The results revealed clear amplification patterns related to topography. PERC1 consistently exhibited higher amplification across events and components, demonstrating that topographic variations – rather than proximity or subtle geological changes – play a critical role in modifying seismic response. These ETF estimates proved valuable for validating and calibrating numerical models, especially in 2D simulations that account for surface geometry.

The rotated HVFSR analysis effectively identified azimuthal variations in amplification, which corresponded well with the steepest slope directions. Stations at the base of slopes (PERC2) exhibited deamplification, while those at hilltops (PERC1) displayed significant amplification, reinforcing findings from previous studies. Nevertheless, the stratigraphic conditions at the PERC2 site, influenced by its proximity to the base of the hill, could also affect the seismic response. Although this technique effectively highlighted directional resonance caused by local topography, it was less informative at sites affected by larger-scale geomorphology (e.g., UTP). Complementary polarization analysis provided further insight into directional effects, especially at UTP, where the rotated HVFSR did not reveal anomalies, but the polarization diagram indicated a preferred azimuth consistent with nearby scarps. The SSR analysis further confirmed topographic amplification and deamplification patterns consistent with studies in similar environments.

Classic tools for seismic response analysis – such as empirical site classification, ETF, and the Kg index – remain valuable, especially when enhanced with directional methods. While local geology governs the primary characteristics of site response, geomorphological features have a more pronounced role in complex terrains. Therefore, we focused on quantifying topographic effects through three complementary approaches. Although additional methods (e.g., damping ratio from borehole sensors or κ_0 estimations) could enhance the analysis, their application was limited by the available data (i.e., surface stations only). Future studies in Colombia and other tectonically active mountainous regions should incorporate similar multi-method frameworks to better understand seismic site response under complex topographic conditions.

Acknowledgements. Colombian public resources supported this work through the Colombian Geological Survey (SGC from Servicio Geológico Colombiano in Spanish) and the Pereira City Hall, completed in the special agreement N° 18 of 2019: "Aunar esfuerzos técnicos, administrativos y financieros para realizar el estudio de actualización y armonización de los estudios de microzonificación sísmica del área urbana y de expansión del municipio de Pereira (Risaralda), así como la evaluación de escenarios de riesgo sísmico". Special acknowledgment to Nelson Perico, Leonardo Santos Mateus, and Helber García, their work and discussions were unvaluable for this work.

Data resources. This work does not aim to publish or replace the microzonation study of Pereira city developed by the SGC and the Pereira city hall, however we used data from the study to develop it. The microzonation study of Pereira, including datasets and geodatabases can be requested directly to the Colombian Geological Survey to cliente@sgc.gov.co.

References

Abdelrahman, K., A. M. Al-Amri, H. Alzahrani, S. Qaysi and N. Al-Otaibi (2022). Soil liquefaction susceptibility of Jizan coastal area, southwest Saudi Arabia, based on microtremor measurements, Arabian Journal of Geosciences, 15, 7, 611, doi:10.1007/s12517-022-09863-0.

Aki, K. (1957). Space and Time Spectra of Stationary Stochastic Waves, with Special Reference to Microtremors, Bull. Earthq. Res. Inst., 35, 415-456.

Akkaya, İ. (2020). Availability of seismic vulnerability index (Kg) in the assessment of building damage in Van, Eastern Turkey, Earthquake Engineering and Engineering Vibration, 19, 1, 189-204, doi:10.1007/s11803-020-0556-z.

Arteta, C. A., C. A. Pajaro, V. Mercado, J. Montejo et al. (2021). Ground-motion model for subduction earthquakes in northern South America, Earthquake Spectra, 37, 4, 2419-2452, doi:10.1177/87552930211027585.

Arteta, C. A., C. A. Pajaro, V. Mercado, J. Montejo et al. (2023). Ground-Motion Model (GMM) for Crustal Earthquakes in Northern South America (NoSAm Crustal GMM). Bull. Seismol. Soc. Am., 113, 1, 186-203, doi:10.1785/0120220168.

Benkaci, N., E. H. Oubaiche, J.-L. Chatelain, R. Bensalem et al. (2021). Non-Stability and Non-Reproducibility of Ambient Vibration HVSR Peaks in Algiers (Algeria), J. Earthquake Engin., 25, 5, 853-871, doi:10.1080/13632469.2018.1537903.

Beyer, K. (2006). Relationships between Median Values and between Aleatory Variabilities for Different Definitions of the Horizontal Component of Motion, Bull. Seismol. Soc. Am., 96, 4A, 1512-1522, doi:10.1785/0120050210.

Beyreuther, M., R. Barsch, L. Krischer, T. Megies et al. (2010). ObsPy: A Python Toolbox for Seismology, Seismol. Res. Lett., 81, 3, 530-533, doi:10.1785/gssrl.81.3.530.

Borcherdt, R. D. (1970). Effects of local geology on ground motion near San Francisco Bay, Bull. Seismol. Soc. Am., 60, 1, 29-61.

Borcherdt, R. D. (1994). Estimates of Site-dependent Response Spectra for Design (Methodology and Justification). Earthquake Spectra, 10, 4, 617-653.

Bradley, B. A. and J. W. Baker (2015). Ground motion directionality in the 2010-2011 Canterbury earthquakes, Earthquake Engin. Strct. Dyn., 44, 3, 371-384, doi:10.1002/eqe.2474.

Building Seismic Safety Council (US). (1988). NEHRP recommended provisions for the development of seismic regulations for new buildings https://www.wbdg.org/FFC/DHS/ARCHIVES/FEMA95_NEHRP_Provisions_Part_1_Provisions_1988.pdf, https://www.wbdg.org/dhs/criteria/fema-95-pt-2-commentary-1988.

Caballero, H. and G. Zapata (1984). Geología y geoquímica de la plancha 224 Pereira, 186, https://www.scribd.com/document/345240133/Memoria-Palncha-IGAC-224.

Cara, F., G. Di Giulio and A. Rovelli (2003). A Study on Seismic Noise Variations at Colfiorito, Central Italy: Implications for the Use of H/V Spectral Ratios, Geophys. Res. Lett., 30,18, doi:10.1029/2003GL017807.

Chávez-García, F., H. Monsalve Jaramillo, M. Gómez Cano and J. Vila Ortega (2018). Vulnerability and Site Effects in Earthquake Disasters in Armenia (Colombia), I – Site Effects, Geosciences, 8, 7, 254, doi:10.3390/geosciences8070254.

Cho, I., S. Senna and H. Fujiwara (2013). Miniature array analysis of microtremors, Geophysics, 78, 1, KS13-KS23, doi:10.1190/geo2012-0248.1.

Cho, I., T. Tada and Y. Shinozaki (2004). A new method to determine phase velocities of Rayleigh waves from microseisms, Geophysics, 69, 6, 1535-1551, doi:10.1190/1.1836827.

Chopra, S., V. Kumar, P. Choudhury and R. B. S. Yadav (2018). Site classification of Indian strong motion network using response spectra ratios, J. Seismol., 22, 2, 419-438, doi:10.1007/s10950-017-9714-9.

Di Alessandro, C., L. F. Bonilla, D. M. Boore, A. Rovelli and O. Scotti (2012). Predominant-period site classification for response spectra prediction equations in Italy. Bulletin of the Seismological Society of America, 102, 2, 680-695. doi:10.1785/0120110084.

Di Giulio, G., F. Cara, A. Rovelli, G. Lombardo and R. Rigano (2009). Evidences for strong directional resonances in intensely deformed zones of the Pernicana fault, Mount Etna, Italy. Journal of Geophysical Research: Solid Earth, 114, 10, doi:10.1029/2009JB006393.

Díaz, F., J. Montejo, N. Perico, L. Mateus et al.(2021). Zonificación de Respuesta Sísmica de Pereira.

Farrugia, J. J., G. M. Atkinson and S. Molnar (2018). Validation of 1D earthquake site characterization methods with observed earthquake site amplification in Alberta, Canada, Bull. Seismol. Soc. Am., 108, 1, 291-308, doi:10.1785/0120170148.

Fukushima, Y., L. F. Bonilla, O. Scotti and J. Douglas (2007). Site classification using horizontal-to-vertical response spectral ratios and its impact when deriving empirical ground-motion prediction equations, J. Earthqu. Engin., 11, 5, 712-724, doi:10.1080/13632460701457116.

Güven, İ. T. (2022). Seismic vulnerability indices for ground in Derince-Kocaeli (NW Turkey), Environ. Earth Sci., 81, 5, 167, doi:10.1007/s12665-022-10288-x.

Hashash, Y. M. A., M. I. Musgrove, J. A. Harmon, O. Ilhan et al. (2020). DEEPSOIL 7.0, User manual. Board of Trustees of University of Illinois at Urbana-Champaign, http://deepsoil.cee.illinois.edu/.

Hillers, G. and Y. Ben-Zion (2011). Seasonal variations of observed noise amplitudes at 2-18 Hz in southern California, Geophys. J. Int., 184, 2, 860-868, doi:10.1111/j.1365-246X.2010.04886.x.

Hudson, B. and I. Idriss (1994). User's Manual for QUAD4M.

Idini, B., F. Rojas, S. Ruiz and C. Pastén (2017). Ground motion prediction equations for the Chilean subduction zone, Bull. Earthquake Engin., 15, 5, 1853-1880, doi:10.1007/s10518-016-0050-1.

International Council of Building Officials (ICBO). (1997). Uniform Building Code, 44, https://www.iccsafe.org/wp-content/uploads/Free%20Codes/Legacy/UBC_IBC_crossref_06.pdf.

Jalil, A., T. F. Fathani, I. Satyarno and W. Wilopo (2021). Liquefaction in Palu: the cause of massive mudflows, Geoenviron. Disasters, 8, doi:10.1186/s40677-021-00194-y.

Jurkevics, A. (1988). Polarization analysis of three-component array data, Bull. Seismol. Soc. Am., 78, 5, 1725-1743.

Kaklamanos, J., L. G. Baise, E. M. Thompson and L. Dorfmann (2015). Comparison of 1D linear, equivalent-linear, and nonlinear site response models at six KiK-net validation sites, Soil Dyn. Earthqu. Engin., 69, 207-219, doi:10.1016/j.soildyn.2014.10.016.

Kang, S. Y., K. H. Kim, Y. S. Gihm and B. Kim (2022). Soil liquefaction potential assessment using ambient noise: A case study in Pohang, Korea, Front. Earth Sci., 10, doi:10.3389/feart.2022.1029996.

Kawase, H., F. Nagashima, K. Nakano and Y. Mori (2019). Direct evaluation of S-wave amplification factors from microtremor H/V ratios: Double empirical corrections to "Nakamura" method, Soil Dyn. Earthqu. Engin., 126, doi:10.1016/j.soildyn.2018.01.049.

Kokusho, T. and K. Sato (2008). Surface-to-base amplification evaluated from KiK-net vertical array strong motion records, Soil Dyn. Earthqu. Engin., 28, 9, 707-716, doi:10.1016/j.soildyn.2007.10.016.

Massa, M., S. Barani and S. Lovati (2014). Overview of topographic effects based on experimental observations: Meaning, causes and possible interpretations, Geophys. J. Int., 197, 3, 1537-1550, doi:10.1093/gji/ggt341.

Meneisy, A. M., M. Toni and A. A. Omran (2020). Soft Sediment Characterization using Seismic Techniques at Beni Suef City, Egypt, J. Environ. Engin. Geophys., 25, 3, 391-401, doi:10.32389/JEEG19-069.

Mercado, V., C. A. Pajaro, C. A. Arteta, F. J. Díaz et al. (2023). Semiempirical model for the estimation of site amplification in Northern South America, Earthquake Spectra, doi:10.1177/87552930231153190.

Nakamura, Y. (2002). Clear identification of fundamental idea of Nakamura's technique and its applications, The 12th World Conf. on Earthquake Engineering, Auckland, New Zealand, 30 January-4 February 2000.

Nakamura, Y. (2019). What is the Nakamura method? Seismol. Res. Lett., 90, 4, 1437-1443, Seismol. Soc. Am., doi:10.1785/0220180376.

Nelson, H. W. (1957). Contribution to the Geology of the Central and Western Cordillera of Colombia in the sector between Ibagué and Cali, Leidse Geologische Mededelingen, 22, 1, 1-75.

Page, W. D. (1984). Popayán, Colombia earthquake of march 31, 1983, Geologic and seismological aspects, Boletines Técnicos AIS, 24.

Pamuk, E., Ö. C. Özdağ, A. Tunçel, S. Özyalın and M. Akgün (2018). Local site effects evaluation for Aliağa/İzmir using HVSR (Nakamura technique) and MASW methods, Nat. Hazards, 90, 2, 887-899, doi:10.1007/s11069-017-3077-y.

Panzera, F., G. Lombardo, D. DAmico and P. Gale (2013). Speedy Techniques to Evaluate Seismic Site Effects in Particular Geomorphologic Conditions: Faults, Cavities, Landslides and Topographic Irregularities, In Engineering Seismology, Geotech. Struct. Earthqu. Engin., InTech, doi:10.5772/55439.

Panzera, F., M. Pischiutta, G. Lombardo, C. Monaco and A. Rovelli (2014). Wavefield Polarization in Fault Zones of the Western Flank of Mt. Etna: Observations and Fracture Orientation Modelling, Pure Appl. Geophys., 171, 11, 3083-3097, doi:10.1007/s00024-014-0831-x.

Pelekis, P. C. and G. A. Athanasopoulos (2011). An overview of surface wave methods and a reliability study of a simplified inversion technique, Soil Dyn. Earthqu. Engin., 31, 12, 1654-1668, doi:10.1016/j.soildyn.2011.06.012.

Pilz, M. and F. Cotton (2019). Does the One-Dimensional Assumption Hold for Site Response Analysis? A Study of Seismic Site Responses and Implication for Ground Motion Assessment Using KiK-Net Strong-Motion Data. Earthquake Spectra, 35, 2, 883-905, doi:10.1193/050718EQS113M.

Pischiutta, M., M. Pastori, L. Improta, F. Salvini and A. Rovelli (2014). Orthogonal relation between wavefield polarization and fast S wave direction in the Val d'Agri region: An integrating method to investigate rock anisotropy, J. Geophys. Res.: Solid Earth, 119, 1, 396-408, doi:10.1002/2013JB010077.

Pischiutta, M., S. Petrosino and R. Nappi (2022). Directional amplification and ground motion polarization in Casamicciola area (Ischia volcanic island) after the 21 August 2017 Md 4.0 earthquake, Front. Earth Sci., 10, doi:10.3389/feart.2022.999222.

Pischiutta, M., F. Salvini, J. Fletcher, A. Rovelli and Y. Ben-Zion (2012). Horizontal polarization of ground motion in the Hayward fault zone at Fremont, California: Dominant fault-high-angle polarization and fault-induced cracks, Geophys. J. Int., 188, 3, 1255-1272, doi:10.1111/j.1365-246X.2011.05319.x.

Posada, G., G. Monsalve, C. D. Hoyos, A. M. Pérez-Hincapié and J. C. Trujillo-Cadavid (2022). Ground accelerations and empirical site classification through H/V response spectral ratio (HVRSR) using historical records from the strong motion network of the Aburrá Valley, Colombia, Soil Dyn. Earthqu. Engin., 152, doi:10.1016/j.soildyn.2021.107063.

Reinoso, E. and M. Ordaz (1999). Spectral Ratios for Mexico City from Free-Field Recordings, Earthquake Spectra, 15, 2, 273-295, doi:10.1193/1.1586041.

Rezaei, S. and A. J. Choobbasti (2014). Liquefaction assessment using microtremor measurement, conventional method and artificial neural network (Case study: Babol, Iran), Front. Struct. Civil Engin., 8, 3, 292-307, doi:10.1007/s11709-014-0256-8.

Servicio Geológico Colombiano. (1993). Red Sismologica Nacional de Colombia [Data set], International Federation of Digital Seismograph Networks, doi:10.7914/SN/CM.

SESAME (2004). Guidelines for the implementation of the H/V spectral ration technique on ambient vibrations measurements, processing and interpretation.

Universidad de los Andes – CARDER (1999). Exploración geotécnica, investigación de laboratorio y microzonifcación sísmica de las áreas urbanas y suburbanas de los municipios de Pereira, Dosquebradas y Santa Rosa de Cabal.

Volant, P., F. Cotton and J. C. Gariel (1998). Estimation of site response using the H/V method. Applicability and limits of this technique on Garner Valley downhole array dataset California), in Proceedings of the 11th European Conference on Earthquake Engineering.

Wathelet, M., J.-L. Chatelain, C. Cornou, G. Di Giulio et al. (2020). Geopsy: A User-Friendly Open-Source Tool Set for Ambient Vibration Processing, Seismol. Res. Lett., 91, 3, 1878-1889, doi:10.1785/0220190360.

Weatherill, G. A., M. Pagani and J. García (2014). OpenQuake Ground Motion Toolkit – User Guide, https://www.globalquakemodel.org/gempublications/openquake-ground-motion-toolkit---userguide.

Zhao, J. X., K. Irikura, J. Zhang, Y. Fukushima et al. (2006). An empirical site-classification method for strong-motion stations in Japan using H/V response spectral ratio, Bull. Seismol. Soc. Am., 96, 3, 914-925, doi:10.1785/0120050124.

***CORRESPONDING AUTHOR: Gustavo POSADA**,
JEOPROBE S.A.S, Bogotá, Colombia
e-mail: gustavo.posada1105@gmail.com